

Article

# Global Analysis of Burned Area Persistence Time with MODIS Data

Andrea Melchiorre and Luigi Boschetti \*

College of Natural Resources, University of Idaho, Moscow, ID 83844, USA; amelchiorre@uidaho.edu

\* Correspondence: luigi@uidaho.edu; Tel.: +1-208-885-6508

Received: 13 April 2018; Accepted: 11 May 2018; Published: 14 May 2018



**Abstract:** Biomass burning causes a non-permanent land cover change (burned area) through the removal of vegetation, the deposition of charcoal and ashes, and the exposure of soil; the temporal persistence of these changes is highly variable, ranging from a few weeks in savannas to years in forests. Algorithms for the generation of moderate-resolution (10–30 m) continental and global burned area maps have been prototyped in an effort to meet the needs of diverse users of fire information. Nevertheless, moderate-resolution sensors have reduced the temporal resolution (e.g., to 16 days for Landsat), which could potentially lead to omission errors, especially in ecosystems where the spectral signal associated with burning disappears quickly and cloud cover limits the number of valid observations. This study presents a global analysis of the burned area persistence time, defined as the duration of the spectral separability of the burned/unburned areas mapped by the MODIS MCD64 Global Burned Area Product. The separability was computed by analyzing time series of normalized burn ratio (NBR) from nadir BRDF-adjusted MODIS reflectances (MCD43 product). Results showed that, globally, the median burned area persistence time was estimated at 29 days, and 86.6% of the global area, as detected by MODIS, can only be detected accurately for up to 48 days. Thus, results indicate that burned area persistence time can be a limiting factor for global burned area mapping from moderate-resolution satellite sensors, which have a low temporal resolution (e.g., Landsat 16 days, Sentinel-2A/B 5 days).

**Keywords:** MODIS; burned area mapping; spectral separability

## 1. Introduction

Fire is a natural component of any ecosystem, and it has effects on vegetation, soil, water and atmospheric composition [1–3]. Fire contributes to the global carbon cycle through the emission of greenhouse gases and aerosols from biomass burning [4,5], and as an agent of ecological change influencing the global vegetation dynamics [6–8] and the surface energy budget [9,10]. Earth Observation (EO) data allow the analysis of biodiversity, dynamics of biomass, productivity, and disturbances spatially from regional to global scales [11]. The application of satellite data to studying vegetation fires has greatly enhanced the possibility of introducing the effect of fire disturbances in global models of climate and atmospheric composition and dynamics estimation [12]. Several studies have used post-fire albedo observations to investigate fire-induced vegetation change impacts on radiative forcing and local effects on climate [9,13,14]. Due to their significant effects on terrestrial ecosystems and atmospheric processes, fire disturbances are included in the list of the required Essential Climate Variables (ECV) in support of the work of the United Nation Framework Convention on Climate Change (UNFCCC) and the Intergovernmental Panel on Climate Change (IPCC) [15].

Burned area maps are defined as the primary variable of the Fire ECV [15], and are currently one of the main inputs for the estimation of atmospheric emissions due to biomass burning [4,15,16].

Systematic global burned area maps at coarse spatial resolution (350 m–1 km) have been produced in the last 20 years from several EO systems, including ATSR, MERIS, MODIS, and SPOT-VGT [17–22]. Burned area coarse-resolution maps have improved the global long-term estimates of fire activity trends [23], and they were used to build fire-related databases of aggregated burned area and emission estimates to help understand the interconnections between fire activity and the global carbon cycle [24]. Such databases include the Global Fire Emissions Database (GFEDv4) [16], the Global Fire Assimilation System (GFAS) [25], the Emission for Atmospheric Chemistry and Climate Model Intercomparison Project (ACCMIP) [26], and the United Nations Food Agriculture Organization (UN-FAO)'s FAOSTAT Emission database [27,28].

Among others, the coarse resolution of the burned area products is a source of uncertainties in these emission databases [4], because it leads to a trade-off between omission and commission errors on partially burned pixels [29]. Pixels classified as burned are considered completely burned, which is often not the case. Due to the heterogeneous nature of fire, sub-pixel unburned patches may exist and result in overestimations of the burned area. Conversely, partially burned pixels can be undetected, resulting in underestimations of the burned area, especially in areas where small fires are common [24,30]. Consequently, there is a strong need for moderate-resolution (10–30 m) global burned area maps for fire and ecosystem management, improved emission estimations, and carbon accounting [30–32].

Automated mapping algorithms using Landsat and Sentinel data are currently being prototyped [33–35] but, among others, one of the challenges of designing a global burned area detection algorithm is the limited temporal resolution of moderate-resolution sensors due to their narrow field of view. The limited number of acquisitions obtained by moderate-resolution satellite translates into potential omission errors [33], because the effects of fire on the spectral signal of vegetation are not permanent. In the days or weeks after a fire, depending on vegetation type, phenology and climate, charcoal and ashes are removed and vegetation recovers [36–40], decreasing the differences of the pre- and post-fire satellite observations over burned areas. Consequently, it is possible to detect burned areas within a limited period, which varies across different ecosystems, and within the same ecosystem, it depends on the timing of the fire. Previously published in situ spectral measurements indicate that the period of detectability of burned areas ranges from about two weeks in African savannas [37,41,42] to more than two years in boreal forests [43]. Similarly, studies using post-fire satellite observations indicate that the spectral changes induced by fire disappear rapidly in grasslands and savannas [37,44,45], but are generally persistent in forested ecosystems [46–48].

The impermanent nature of the spectral signal associated with burned areas poses a major challenge for designing a global burned area mapping algorithms from moderate resolution satellites [33]. For example, Landsat satellites have a 16-day revisit time, and the newly available Sentinel-2A and Sentinel-2B have 10-day revisit times (5 days when both satellites are used in combination), which can be a limiting factor for global burned area mapping from moderate-resolution satellite sensors. Burned area mapping algorithms require at least one cloud-free acquisition before and after the fire event; and, using moderate-resolution data, omission errors might result in areas where the spectral signal associated with burning disappears quickly due to the lower revisit frequency. This work presents the first global, systematic temporal analysis of the spectral signal associated to burned areas and the relative persistence time in order to determine the length of the period in which the burned class is spectrally distinct from the unburned and, therefore, detectable.

The burned area persistence time was estimated as the maximum number of days in which the values of the spectral index Normalized Burn Ratio associated to burned and unburned areas are separable and, therefore, burned areas can be mapped reliably. The primary input of the study was provided by 14 years of the MODIS burned area and surface reflectance products, from January 2003 to December 2016, in order to use every full year for which both MODIS-Terra and MODIS-Aqua data are available. The analysis was stratified spatially by ecoregions and land cover, and temporally considering the period of the year in which the fire occurred. Nadir Bidirectional Reflectance

Distribution Function (BRDF)-adjusted reflectance product (MCD43A4) time series of burned pixels, as detected by the MODIS global burned area product (MCD64A1), within the same ecoregion and land cover were used to characterize the pre- and post-fire temporal variations with the passing of time due to dissipation charcoal and ashes, vegetation regrowth, and snow cover. Reflectance time series of unburned pixels within the same ecoregion and land cover were used to characterize the variations in reflectance due to vegetation phenology and other disturbances. Summary metrics were defined for reporting the results at the global scale, aggregating by global biome and realm.

The paper is organized as follows. Section 2 describes the satellite datasets used for the analysis, and the ancillary datasets used as stratification variables. Section 3 describes the methods, establishing a rigorous probabilistic framework for the definition of the persistence time of burned areas at different scales, and presenting the formulae needed for a global, multiyear analysis. Section 4 presents the results and Section 5 discusses the differences observed across land cover types, biomes and realms. The paper concludes with recommendations for future research and application.

## 2. Data

### 2.1. MODIS Global Burned Area Product

The most recent Collection 6 MODIS Global Burned Area Product (MCD64A1) provides the estimated date of burn for the 500 m MODIS pixels that are classified as burned to within a calendar month [18,19]. The global monthly MCD64A1 data record from 2003 to 2016 was used, in order to include every full year in which both MODIS instruments—on the Terra and Aqua platforms—were operating. The algorithm [18] was designed to be extremely tolerant of cloud and aerosol contamination, which affected the Collection 5 MODIS 500 m burned area product [49]. The algorithm applies dynamic thresholds to composite MODIS Terra and Aqua imagery generated from a burn-sensitive spectral band index derived from MODIS 1240 nm and 2130 nm Terra and Aqua bands, and a measure of temporal variability. Cumulative MODIS 1 km active fire detections are used to guide the selection of burned and unburned training samples and to guide the specification of prior burned and unburned probabilities. The MCD64A1 product is distributed in the standard MODIS Level 3  $10^\circ \times 10^\circ$  Land tile format in the sinusoidal projection [50].

### 2.2. MODIS Global Nadir BRDF-Adjusted Reflectance Product

The MODIS Nadir BRDF-Adjusted Reflectance (NBAR) product provides estimates of the nadir surface reflectance at local solar noon performing a Bidirectional Reflectance Distribution Function (BRDF) inversion of MODIS surface reflectance for each day using a 16-day moving window centered on the nominal product date [51,52]. The Collection 6, Level 3 daily MODIS Terra and Aqua combined product (MCD43A4) was used in this work. The MCD43A4 product is defined in the MODIS Level 3 Land tile format in sinusoidal projection at 500 m resolution. Per-pixel quality assessment information is provided by the MCD43A2 product, also defined in the MODIS Level 3 Land tile format in sinusoidal projection at 500 m resolution and, for each reflective band of the MCD43A4 product, reports the quality of the BRDF inversion for each pixel of the relative MCD43A4 product, and flags the presence of water and snow pixels.

### 2.3. MODIS Land Cover Product

The MODIS Land Cover Type product (MCD12Q1) provides five land classification schemes, which describe land cover properties derived from one year of observations from Terra- and Aqua-MODIS [53]. The Collection 5.1, Level 3 yearly land cover product is defined in the MODIS Level 3 Land tile format in sinusoidal projection at 500 m resolution. The International Geosphere and Biosphere Programme (IGBP) scheme, which identifies 16 land cover classes, including 11 natural vegetation classes, 3 developed and 2 non-vegetated land classes, and has a reported 75% overall land cover classification accuracy [53], was used in this work.

## 2.4. Terrestrial Ecoregions of the World

The Terrestrial Ecoregions of the World (TEOW) map is a biogeographic division of the Earth's terrestrial biodiversity into 867 ecoregions, which belong to 14 biomes and 8 realms [54]. Ecoregions are defined as biogeographic units containing a homogeneous population of natural communities (flora and fauna) sharing a large majority of species, dynamics, and environmental conditions.

## 3. Methods

### 3.1. Theoretical Basis: Definition of the Burned Area Persistence Time

The burned area persistence time was defined as the maximum time after a fire during which burned pixels can be unambiguously separated from unburned ones (i.e., the length of the period in which burned areas can be reliably mapped).

The spectral signature of vegetation is altered by burning events, and the magnitude of these changes is greater in some portions of the electromagnetic spectrum than in others. It has been demonstrated that the spectral bands more suitable for burned area mapping are the near infrared (NIR) and shortwave infrared (SWIR) for both coarse- [55–57] and moderate-resolution satellites [58–61]. The spectral changes induced by fire are non-permanent; charcoal and ashes are removed by atmospheric agents exposing the bare soil, and vegetation regrows over time [62]. Additionally, the spectral signature of unburned pixels also changes over time: vegetation phenology, senescence and other disturbances, such as forest management thinning and clear cuts, mortality due to insect outbreaks and land use conversion, cause spectral changes that can be confused with those due to fire [63,64]. For these reasons, burned area spectral separability is sensitive to the time elapsed since the burning event [19,44,65]; the detectability of burned areas is a function—among other factors—of the burned area persistence time.

A wide variety of burned area mapping algorithms have been tested and developed for moderate resolution sensors including techniques that exploit single image analysis [66–70] and multi-temporal analysis [33,59,66,71–75]. Although there is no agreement on the optimal burned area mapping algorithm, spectral indices are widely used in many studies. Among them, the Normalized Burn Ratio (NBR [76]) is widely used for burned area detection with moderate resolution satellite data [67,69,71,73–75,77,78]. The index range is between  $-1$  and  $1$ , and it is defined as:

$$\text{NBR} = \frac{\rho_{\text{NIR}} - \rho_{\text{SWIR}}}{\rho_{\text{NIR}} + \rho_{\text{SWIR}}} \quad (1)$$

where  $\rho_{\text{NIR}}$  is the reflectance at  $0.8 \mu\text{m}$  and  $\rho_{\text{SWIR}}$  is the reflectance at  $2.1 \mu\text{m}$ . The difference between pre-fire and post-fire NBR (dNBR) is an indication of the spectral changes due to fire. dNBR can assume values between  $-2$  and  $2$ . Because NBR drops after a fire due to the removal of vegetation, soil exposure and charcoal and ash deposition [58], positive dNBR values are associated with burning, thus making dNBR thresholding a simple burned area detection strategy [75,76,79].

In this study, daily time series of dNBR were generated for burned and unburned pixels from the Nadir BRDF-Adjusted Reflectance Albedo product (MCD43A4) to minimize the variability in reflectance due to different acquisition view geometry. Missing data, and water- and snow-covered pixels were discarded from further analysis.

For burned pixels at a generic location  $i$  that were detected as burned on Julian day of the year  $j_{\text{doy}}$  in the MODIS global burned area product (MCD64A1), the post-fire dNBR yearly time series was defined as:

$$\text{dNBR}_B(\Delta t)_{i,j_{\text{doy}}} = \text{NBR}_{i,j_{\text{doy}}-8} - \text{NBR}_{i,j_{\text{doy}}+\Delta t} \quad (2)$$

where  $\text{NBR}_{i,j_{\text{doy}}-8}$ , is the pre-fire NBR value, obtained from the MCD43A4 product with the nominal date 8 days before the day  $j_{\text{doy}}$  of burning, and  $\text{NBR}_{i,j_{\text{doy}}+\Delta t}$  is the value observed  $\Delta t$  days after the fire, with  $\Delta t \geq 8$ . The 16-day minimum time difference between pre-fire and post-fire observation was

required to account for the 16-day inversion moving window used in the MCD43A4 product and to ensure that the NBR pre-fire and post-fire values were respectively calculated only from the inversion of pre-fire and post-fire reflectances.

Generally, the spectral signature of vegetation varies during the year depending on phenology (e.g., senescence, leaf-off) and stress conditions; as a result, the NBR of unburned vegetation is variable during the year. Equation (2) generates yearly time series of dNBR measuring only the changes from the pre-fire conditions, regardless of the initial NBR value.

Similarly, a generic unburned pixel  $j$ , observed synchronously with the burned pixel  $i$  of Equation (2), will describe spectral temporal variations determined by vegetation phenology and other non-fire-related factors:

$$\text{dNBR}_{UB}(\Delta t)_{j,jdoy} = \left[ \text{NBR}_{j,jdoy-8} - \text{NBR}_{j,jdoy+\Delta t} \right] \quad (3)$$

where  $\text{NBR}_{j,jdoy-8}$  is the NBR value of the unburned pixel  $j$  on the same pre-fire date of Equation (2), and  $\text{NBR}_{j,jdoy+\Delta t}$  is the value observed  $\Delta t$  days after the starting day  $jdoy$ .

Considering a set of burned pixels  $ba$ , all burning on the same day  $jdoy$ , the individual trends of Equation (2) were aggregated in a probability distribution function:

$$P_B(\text{dNBR})_{\Delta t,jdoy} = P(\text{dNBR}_B(\Delta t)_{i,jdoy} = \text{dNBR}, i \in ba) \quad (4)$$

This is illustrated in Figure 1. Considering a set of burned pixels detected on the same day  $jdoy$  in one spatial stratum of the analysis ('Victoria Plains tropical savanna' ecoregion in Northern Australia, savanna land cover), the histogram of the distribution  $P_B(\text{dNBR})_{\Delta t,jdoy}$  is represented by the dashed red lines. Notably, the range of dNBR values assumed by the burned area increases as time from the fire (i.e.,  $\Delta t$ ), indicating heterogeneous post-fire trajectories, and the median value decreases, indicating a tendency to return to pre-fire conditions. The post-fire spectral signature varies depending on atmospheric events and vegetation regrowth following the fire; for example, wind and rain can scatter the charcoal and ashes, or a new layer of grasses can grow rapidly after a fire; these effects can have great variability also within the same burned area, resulting in a wider range of post-fire dNBR values.

Similarly, considering a set of unburned pixels  $ua$ , the individual trajectories of Equation (3) were also aggregated into a probability distribution:

$$P_{UB}(\text{dNBR})_{\Delta t,jdoy} = P(\text{dNBR}_{UB}(\Delta t)_{j,jdoy} = \text{dNBR}, j \in ua) \quad (5)$$

In Figure 1, the histogram of the distribution of  $P_{UB}(\text{dNBR})_{\Delta t,jdoy}$  for a set of unburned pixels in the same analysis stratum, and observed from the same day  $jdoy$  as the burned pixels, is represented by the dashed blue line. The range of dNBR values assumed by the unburned pixels also increases with  $\Delta t$ , while the median remains stable around 0, indicating that the set of the unburned pixels shows increasingly heterogeneous trends as time passes; while some pixels show trends that cannot be confused with burning (i.e., negative dNBR changes), others do (i.e., positive dNBR changes), likely due to senescence and phenology.

The separability of burned/unburned pixels was measured in terms of the overlapping portion of the  $P_B(\text{dNBR})_{\Delta t,jdoy}$  and  $P_{UB}(\text{dNBR})_{\Delta t,jdoy}$  distributions. As a result of the temporal variation, the overlap of the two distribution is minimal immediately after the fire, and increases as time passes, reflecting the fact that burned areas can be mapped reliably only for a limited time after the fire. The persistence time of the burned area was, therefore, estimated as the maximum number of days in which the two distributions have minimal or no overlap, and more specifically the number of days in which at least 90% of the burned area pixels have dNBR higher than 90% of the unburned pixels. Using this empirical threshold, the burned area persistence time was estimated as the number of days on which the two distributions overlapped by 20%.

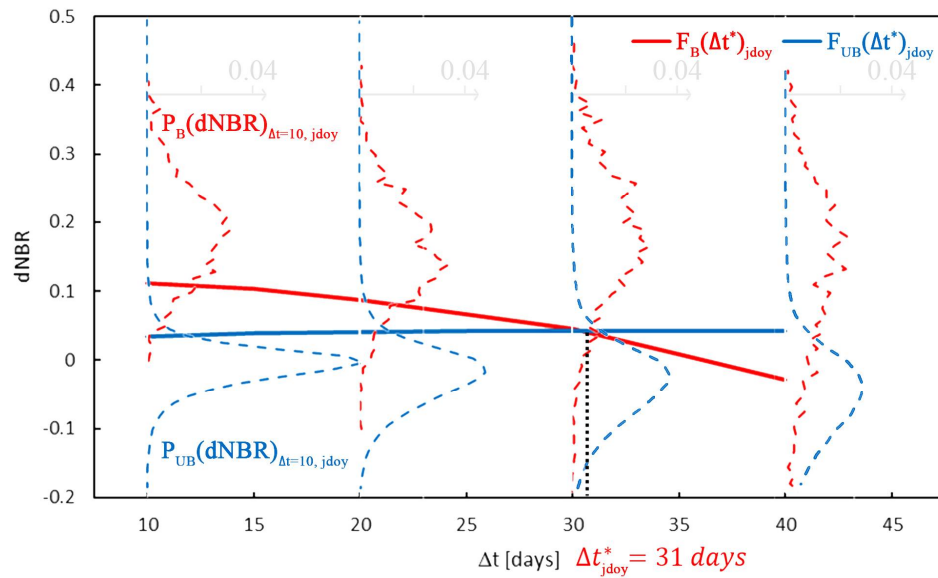


**Figure 1.** Illustration of the method for the estimation of the burned area persistence time. The plot is generated using observations of a set of burned pixels (*ba*) and unburned pixels (*ub*) in the Savanna land cover of the “Victoria Plains tropical savanna” ecoregion in northern Australia, starting on the day of detection of the burned pixels ( $jday = 329$ , November 25th). The red dotted lines show the distribution of dNBR of the burned pixels ( $P_B(dNBR)_{\Delta t, jday}$ ), observed at  $\Delta t = 10, 20, 30$  and  $40$  days after burning; the blue dotted lines show the distribution of dNBR of the unburned pixels ( $P_{UB}(dNBR)_{\Delta t, jday}$ ) observed at the same time. The red and blue solid lines represent respectively the 10th percentile of the dNBR distribution of burned pixels (i.e.,  $F_B(\Delta t)_{jday}$ ) and the 90th percentile of the dNBR distribution of the unburned pixels (i.e.,  $F_{UB}(\Delta t)_{jday}$ ). The persistence time is calculated as the time  $\Delta t^*_{jday}$  when the two distributions overlap by more than 20%, i.e., when  $F_B(\Delta t)_{jday}$  is equal to  $F_{UB}(\Delta t)_{jday}$  ( $\Delta t^*_{jday} = 31$  days in this example).

By definition, 90% of the burned area pixels have a dNBR value higher than the 10th percentile of the  $P_B(dNBR)_{\Delta t, jday}$  distribution, which, expressed as a function of  $\Delta t$ , is defined as:

$$F_B(\Delta t)_{jday} = \text{dNBR} : \left\{ \int_{-2}^{\text{dNBR}} P_B(dNBR)_{\Delta t, jday} = 0.10 \right\} \quad (6)$$

Similarly, 90% of the unburned pixels have a dNBR value lower than the 90th percentile of the  $P_{UB}(dNBR)_{\Delta t, jday}$ :

$$F_{UB}(\Delta t)_{jday} = \text{dNBR} : \left\{ \int_{-2}^{\text{dNBR}} P_{UB}(dNBR)_{\Delta t, jday} = 0.90 \right\} \quad (7)$$

Finally, the persistence time of the burned areas was estimated as the number of days  $\Delta t^*_{jday}$  in which  $F_B(\Delta t)_{jday}$  is greater or equal to  $F_{UB}(\Delta t)_{jday}$ :

$$\Delta t^*_{jday} = \max(\Delta t : F_B(\Delta t)_{jday} \geq F_{UB}(\Delta t)_{jday}) \quad (8)$$

In Figure 1,  $F_B(\Delta t)_{jday}$  and  $F_{UB}(\Delta t)_{jday}$  are represented by the solid red and blue lines, respectively, and the persistence time  $\Delta t^*_{jday}$  is defined by the intersection of the two lines.

### 3.2. Global Implementation

The probabilistic method described in Section 3.1 was implemented globally using the 14 years of MODIS datasets described in Section 2 as shown in Figure 2. Because of the analysis scale, it was

first necessary to stratify the analysis spatially and temporally using strata sufficiently fine to capture the variability of the burned areas, limiting it to the times of the year where fire occurs (Section 3.2.1), and to define a sampling strategy to extract a representative set of burned and unburned pixels within each stratum (Section 3.2.2). The equations of Section 3.1 were then used to build a set of summary metrics at the level of each ecoregion (Section 3.2.3) and globally at the biome scale (Section 3.2.4).

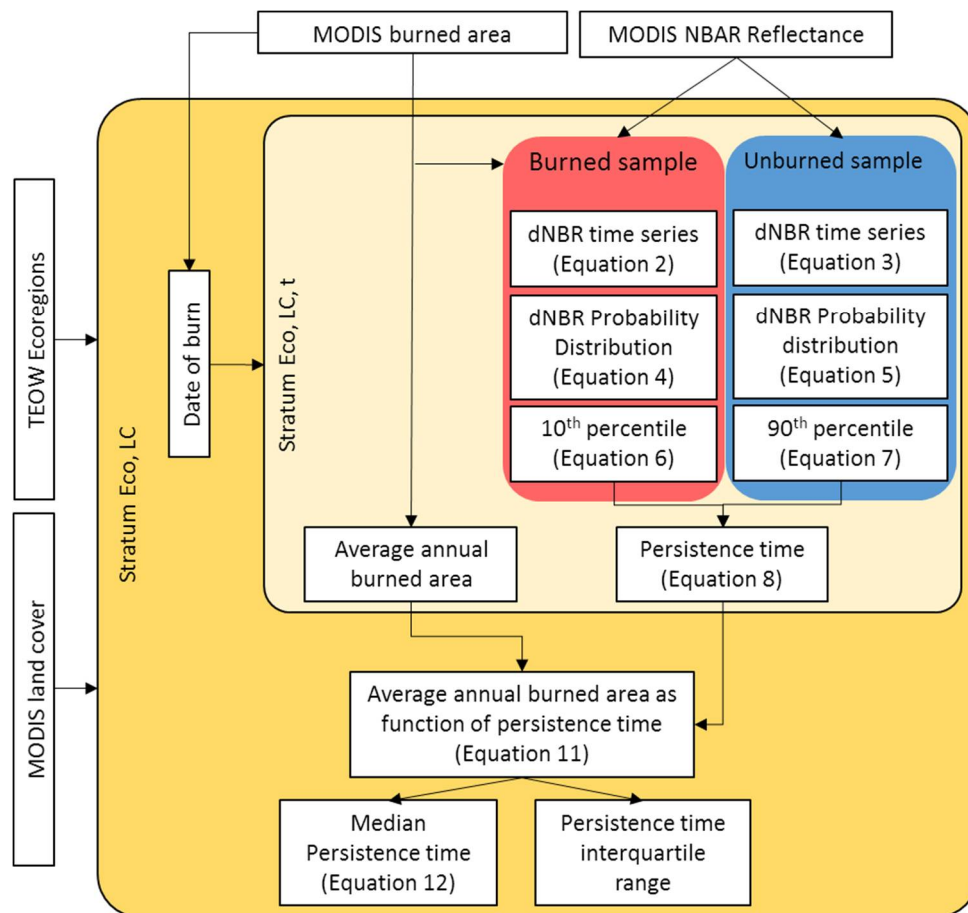


**Figure 2.** Illustration of the procedure for the estimation of the burned area persistence time. The input data for the analysis are the MODIS burned area and NBAR product. The MODIS land cover product and the TEOW ecoregions are used to define each spatial stratum defined by ecoregion and land cover. The estimated burned date extracted from the MODIS burned area product is used to allocate the pixels in the different 16-day periods (Section 3.2.1). The median persistence time for each ecoregion and land cover is computed as the median value of the average annual burned area as a function of the persistence time (Section 3.2.3).

### 3.2.1. Spatial and Temporal Stratification of the Analysis

#### Spatial Stratification

Burned areas have different spectral responses depending on the type and condition of fuels, and more broadly depending on the ecosystem and time of burning [9,45,80], the analysis was performed using spatial and temporal units sufficiently fine to capture such variability. The analysis was stratified spatially adopting a two-level stratification. The Terrestrial Ecoregions of the World (TEOW) [54] were used to define the first stratification level. Ecoregions are delineated according to endemic genera and families (higher taxa), distinct assemblages of species, and the influence of geological history, such as past glaciations, on the distribution of plants and animals [54]. Consequently, they are more likely to accurately reflect the distribution of species and communities than alternative stratifications derived

solely from biophysical variables, such as rainfall and temperature, vegetation structure, or spectral signatures from remote sensing data [54].

The TEOW map is a broad simplification of the variability of habitats, and all contain a variety of vegetation types [54]; for example, boreal ecoregions include forests, shrublands, and grasslands. Consequently, the MODIS MCD12Q1 land cover product was used to define a second level of stratification within each TEOW ecoregion. The land cover classes of the IGBP classification scheme were aggregated into three major classes of interest (Forest, Shrubland, Grassland & Savanna), or masked out and removed from the subsequent analysis (urban areas, croplands, and miscellaneous non-burnable surfaces) (Table 1).

**Table 1.** Land cover aggregation scheme of the MODIS MCD12Q1 IGBP land cover classes used for the present study.

IGBP Land Cover	Aggregated Land Cover
Evergreen Needleleaf forest Evergreen Broadleaf forest Deciduous Needleleaf forest Deciduous Broadleaf forest Mixed forest	Forest
Closed shrublands Open Shrublands	Shrubland
Woody savannas Savannas Grasslands	Grassland & Savanna
Permanent wetlands Croplands Urban and built-up Cropland/Natural vegetation mosaic Snow and ice Barren and sparsely vegetated	Not considered

The spatial strata  $\{Eco, LC\}$ , defined by the generic land cover class  $LC$  within the generic ecoregion  $Eco$ , in which at least 250 km<sup>2</sup> of burned areas were cumulatively detected by the MCD64A1 product over the entire 14 year study period (2003–2016) were considered, thus excluding land cover class/ecoregion combination with negligible fire activity.

#### Temporal Stratification and Temporal Extent of the Analysis

Fire activity is mainly driven by fuel abundance and structure and by climatic conditions that result in changes in fuel moisture and lightning activity [81]. Consequently, different regions of the globe have distinct fire seasons. At the global scale, the fire season peak months in the Southern hemisphere are August–September, primarily driven by the extensive burning in Southern Africa and Australia, while in the Northern hemisphere the peak months are December–January, due primarily to burning across Northern and Central Africa [82]. At the regional scale, fire seasons vary in terms of length, peak activity and numbers of peaks [83]. These differences are linked mainly to the different climatic and the pre-burning fuel conditions, which vary during the fire season [84,85]. Generally, early season fires burn living, photosynthetically active vegetation, and dead vegetation that has a higher moisture content. During the dry season, vegetation senescence and climatic conditions lead to dryer living and dead vegetation [86,87]. As a result, fire-induced spectral changes for a given ecosystem and land cover vary within the fire season [85,88,89].

In order to account for these variations, a temporal stratification grid was created by dividing the January–December calendar year into 23 periods of 16 days each ( $t$ ) (the last period being 13 days). This 16-day temporal grid—which coincides with the return interval of the Landsat satellite—was

sufficiently fine to characterize the spectral temporal variations of burned areas at different times of the year, while significantly reducing the computational load of a daily temporal grid.

To further reduce the computational load, only burned areas occurring during the fire season of each ecoregion were considered. The fire season of each ecoregion was defined by adapting the method proposed by Archibald, Lehmann, Gómez-Dans and Bradstock [84]. Each of the 16-day periods of the year was ranked based on the average annual burned area detected by the MCD64A1 product, and the fire season was defined as the union of the periods in which 90% of the annual burned area is detected. This definition requires no assumption on the continuity of the fire season and is applicable to ecoregions having a variety of temporal patterns of fire activity (Figure 3).

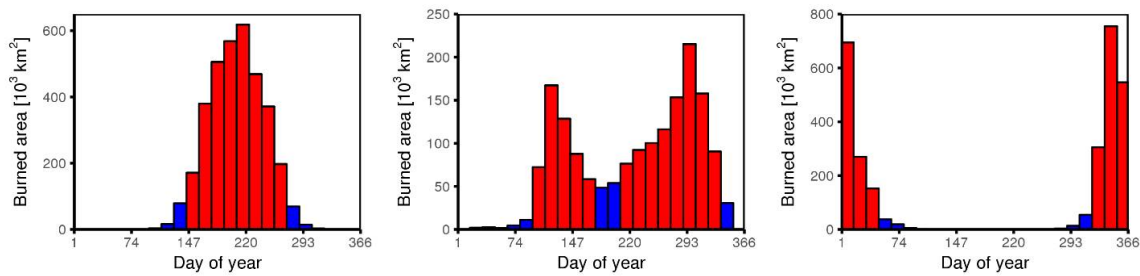


**Figure 3.** Illustration of the procedure for the definition of the fire season, showing the burned area histogram, binned in 16-day intervals  $t$ , of three representative examples of fire season. **Left**, unimodal fire season fully contained in a single calendar year (“Angolan woodland” ecoregion in Southern Africa); **center**, bimodal fire season (“Victoria Plains tropical savanna” ecoregion in northern Australia); **right**, unimodal fire season spanning across calendar years (“Northern Congolian tropical forest-savanna mosaic” ecoregion in northern Africa). The fire season is identified by ranking the 16-day bins in decreasing order by burned area and including in the fire season the bins necessary to reach 90% of the burned area (shown in red). The 16-day periods outside the fire season (shown in blue) were not considered in the analysis.

### 3.2.2. Sampling Design

The MODIS MCD64A1 global burned area product detects, on average,  $\sim 4.0 \times 10^6$  km<sup>2</sup> of burned areas per year [16], corresponding to  $\sim 16 \times 10^6$  pixels per year. To make the analyses logistically possible, a sampling strategy was employed to sample both burned and unburned pixels in the spatial and temporal strata  $\{Eco, LC, t\}$  defined above as a combination of ecoregions, land cover classes, and time of the year quantized in 16-day periods.

The total sample size in each ecoregion was 100,000 burned and 100,000 unburned pixels (or the entire population if fewer than 100,000 pixels exist in either class). This total sample size was then allocated to the spatial sub-strata (i.e., land cover classes with fire activity in the ecoregion) and temporal strata (i.e., number of 16-day periods of the fire season) proportionally to the area burned, and the sample was extracted randomly with no replacement.

Under stratified random sampling, the probability of inclusion is constant within each stratum and is:

$$\pi_h = \frac{n_h}{N_h} \quad (9)$$

where  $n_h$  and  $N_h$  are, respectively, the sample size and the population size in stratum  $h$ .

It follows that within each stratum (i.e., each combination of ecoregion  $Eco$ , land cover  $LC$ , and 16-day period  $t$ ) the inclusion probability was:

$$\pi_{Eco,LC,t} = \frac{ba_{Eco,LC,t}}{BA_{Eco,LC,t}} \quad (10)$$

where  $ba$  is the extracted sample, and  $BA$  is the total population of the burned area in the stratum. It should be noted that the sample  $ba_{Eco,LC,t}$  was drawn from the total population of burned areas detected in ecoregion  $Eco$  and land cover  $LC$ , burned in the 14 years of the study period in the same 16 days of the calendar year defined by the interval  $t$ .

### 3.2.3. Ecoregion Level Estimation of the Persistence Time

The persistence time is estimated for each stratum, by applying Equations (1)–(8) using the sample of burned pixels  $ba_{Eco,LC,t}$  and unburned pixels  $ub_{Eco,LC,t}$ . It should be noted that the 16-day grid was used solely for the stratification of the sample, whereas the variation over time of the dNBR values (Equations (2) and (3)) was evaluated based on the daily MCD43A4 time series. As a consequence, for each land cover and ecoregion, up to 23 persistence times (one for each 16-day period  $t$ ) were obtained, each of them estimated from Equation (8) with daily resolution. This is exemplified in Figure 4 (top), showing the burned area persistence time for the TEOW “Victoria plains tropical savanna” in Northern Australia. The 16-day periods included in the fire season are shaded in gray, and for each of them, the estimated persistence times  $\Delta t^*_{Eco,LC,t}$  in “Shrubland” and “Grassland and Savannah” land cover classes are shown in gray and orange respectively. The persistence time was not computed for the “Forest” land cover, because no time period  $t$  had the minimum number of burned area detections defined in Section 3.2.1.

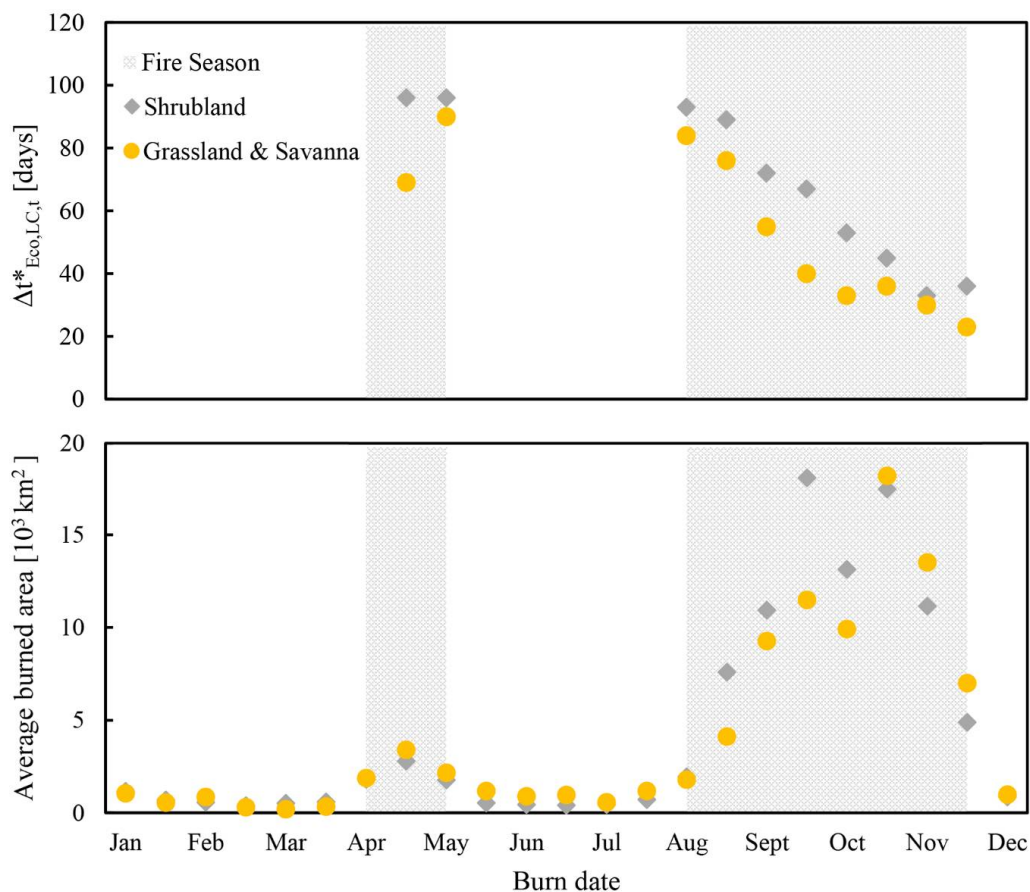


**Figure 4.** Burned area persistence time as a function of the day of burning  $\Delta t^*_{Eco,LC,t}$  (top) and average annual burned area for each 16-day period of the year (bottom), in the “Victoria Plains tropical savanna” ecoregion in Northern Australia, stratified by aggregated land cover class. The persistence time was defined only for the 16-day periods of the fire season (hatched gray area). The Forest land cover class was not considered in this ecoregion because of negligible fire activity (i.e., less than  $250 \text{ km}^2$  over the entire study period).

In order to obtain meaningful summary metrics of the persistence time  $\Delta t^*_{Eco,LC,t}$ , it was necessary to first take into consideration the actual area burned in each time period  $t$  (reported in Figure 4, bottom) for the same ecoregion and land cover, and define an appropriate set of weights. This was done by estimating—in each ecoregion and land cover class—which proportion of the total burned area had a given persistence time  $\Delta t^*_{Eco,LC,t}$ .

The average annual burned area with persistence time  $\Delta t^*$  was estimated as follows:

$$\hat{B}A_{Eco,LC}(\Delta t^*) = \frac{1}{n} \sum_{t=1}^{23} \frac{ba_{Eco,LC,t}}{\pi_{Eco,LC,t}} \delta_{\Delta t^*_{Eco,LC,t}}(\Delta t^*) \tag{11}$$

where  $n$  is the number of years used in the analysis,  $\delta_{\Delta t^*_{Eco,LC,t}}(\Delta t^*)$  is the Dirac measure assuming value 1 if the persistence time for stratum  $\{Eco, LC, t\}$  is equal to  $\Delta t^*$  and 0 elsewhere,  $ba_{Eco,LC,t}$  is the area of the sample extracted from each stratum, and  $\pi_{Eco,LC,t}$  is the inclusion probability defined as in Equation (10). Figure 5 (top) presents the histogram of  $\hat{B}A_{Eco,LC}(\Delta t^*)$  obtained from the persistence times and average area burned of Figure 4.

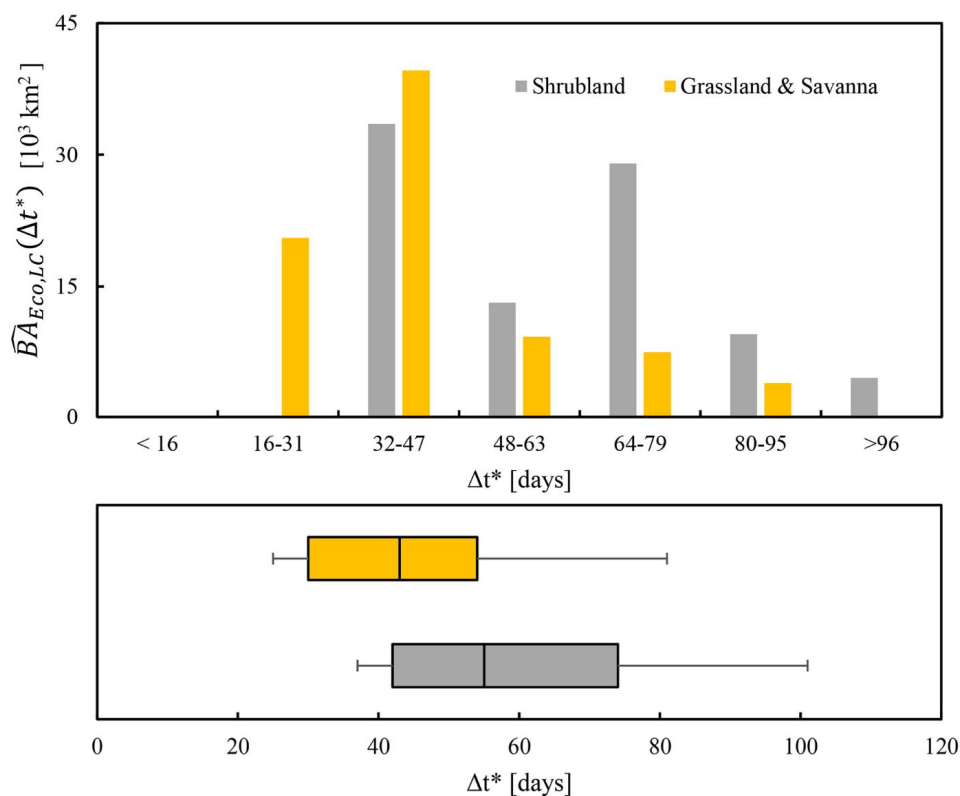


**Figure 5.** Summary persistence time metrics at the ecoregion level, in the “Victoria Plains tropical savanna” ecoregion in Northern Australia, stratified by aggregated land cover class. **Top:** Histogram of  $\hat{B}A_{Eco,LC}(\Delta t^*)$ , i.e., the average annual burned area as a function of the burned area persistence time. The histogram is computed using 16-day bins. **Bottom:** boxplot of  $\hat{B}A_{Eco,LC}(\Delta t^*)$ , showing the median (i.e.,  $\hat{\Delta t^*}_{Eco,LC}$ ), interquartile range, minimum and maximum of the distribution.

Finally, the estimated persistence time for each spatial stratum  $\{Eco, LC\}$  was the time corresponding to the 50th percentile of  $\hat{B}A_{Eco,LC}(\Delta t^*)$ :

$$\hat{\Delta t^*}_{Eco,LC} = \Delta t^* : \left\{ \int_0^{\Delta t^*} \hat{B}A_{Eco,LC}(\Delta t^*) = 0.5 \right\} \tag{12}$$

Additionally, the interquartile range was computed as the difference between the 25th and 75th percentile of  $\widehat{BA}_{Eco,LC}(\Delta t^*)$ , and used to measure the variability of the burned area persistence time within each spatial stratum. Figure 5 (bottom) shows the estimated median persistence time (Equation (12)) and the interquartile range for the ecoregion Victoria plains tropical savanna for the two land covers Shrubland and Grassland & Savanna. In this ecoregion, the estimated persistence time  $\widehat{\Delta t}_{Eco,LC}^*$  was longer for Shrubland land cover (55 days), and 50% of the burned area had an estimated persistence between 42 and 74 days. In comparison, Grassland & Savanna burned area had a shorter persistence (43 days) and variability (interquartile range of 30–54 days).

### 3.2.4. Spatial Aggregation by Land Cover and BIOME/Realm

Because of the large number of spatiotemporal strata, it was necessary to summarize the persistence time results meaningfully in order to present and discuss them. The results were first summarized at the ecoregion level by use of the estimated median persistence time ( $\widehat{\Delta t}_{Eco,LC}^*$ , Equation (12)) and interquartile range, and then spatially aggregated by merging the ecoregions into larger spatial units based on Olson's biomes and realms (Australasia, Antarctic, Afrotropic, Indo-Malay, Neoafrican, Neotropic, Oceania, Palearctic) (Figure 6).

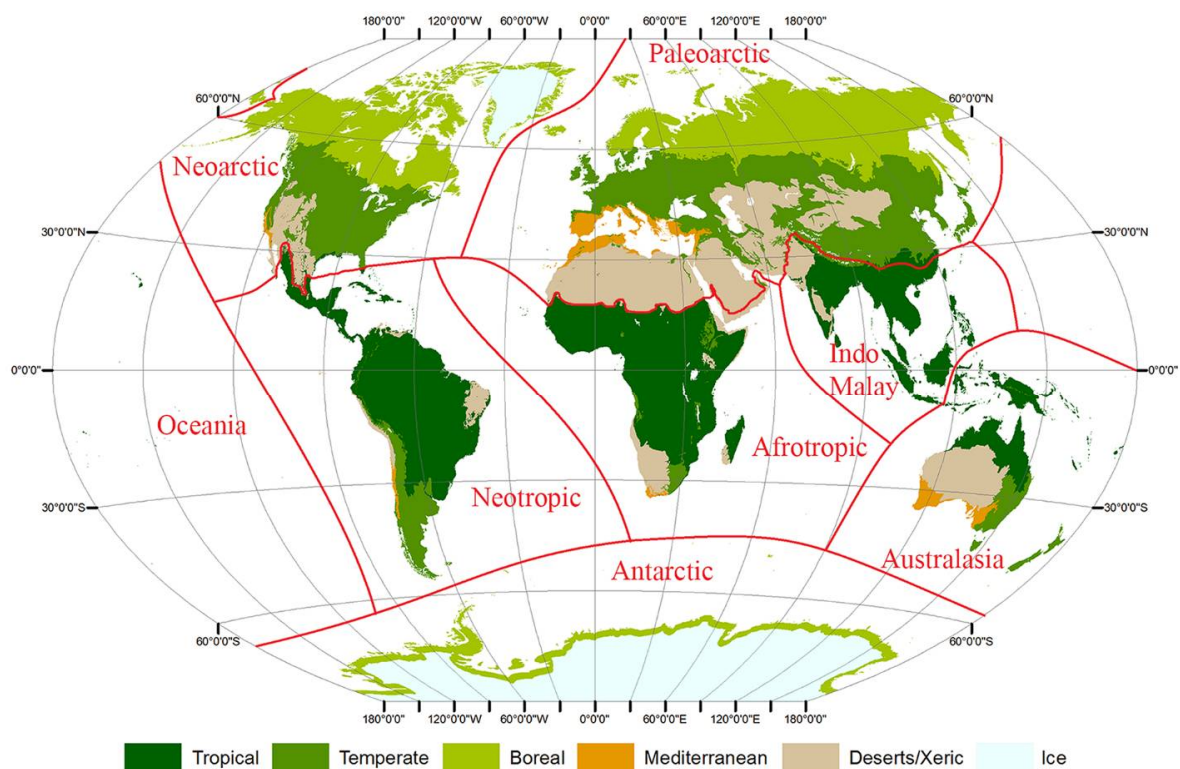


**Figure 6.** Realms and aggregated biomes used as spatial units to present the global summary metrics persistence time. Oceania and Antarctic realms (in gray) were not considered, because of negligible fire activity.

Realms provide a subdivision of the main landmasses, and biomes are a convenient stratification unit because of their homogeneity of climate and vegetation and because “they provide a framework for comparisons among units and the identification of representative habitats and species assemblages” [54]. The TEOW biomes have been used to stratify studies for vegetation mapping [90] and animal species distributions [91], climatic models [92,93], anthropogenic urban growth [94], deforestation [95] and, recently, for the validation of remote sensing global burned area products [96,97]. Following the approach from Boschetti, Stehman and Roy [96], the 14 Olson

biomes were aggregated into 5 more general biomes: Tropical, Temperate, Boreal, Mediterranean and Desert/Xeric biomes (Table 2).

**Table 2.** Biome aggregation scheme of the Olson et al. [54] biomes used for the present study.

Olson Biome	Aggregated Biome
Tropical and subtropical moist broadleaf forest Tropical and subtropical dry broadleaf forest Tropical and subtropical coniferous forest Tropical and subtropical grasslands, savanna Flooded grasslands, savanna (Latitude < 23°) Mangroves	Tropical
Temperate broadleaf and mixed forest Temperate coniferous forest Temperate grasslands, savanna Flooded grasslands, savanna (Latitude > 23°) Montane grasslands, savanna	Temperate
Boreal forest/Taiga Tundra	Boreal
Mediterranean forests, woodlands, and shrublands	Mediterranean
Deserts and xeric shrublands	Desert/Xeric

The realms of Oceania and Antarctica were excluded from the analysis because of the lack of significant fire activity. Of the 30 possible combinations of the remaining 6 realms and 5 biomes, 25 were valid (the Boreal biome is present only in the Paleoarctic and Neoarctic realms and the Mediterranean biome is not present in the Indo-Malay realm) and were adopted as aggregated spatial units for the summary of the analysis results (Figure 6).

The distribution of annual burned area as a function of the spectral signal persistence time  $\Delta t^*$  for each spatial unit defined by Biomes ( $B$ ), Realms ( $R$ ), and land cover ( $LC$ ) was simply calculated by summation of all the ecoregions belonging to the spatial unit, and globally by summation over the realms:

$$\widehat{BA}_{B,R,LC}(\Delta t^*) = \sum_{Eco \in R,B} \widehat{BA}_{Eco,LC}(\Delta t^*) \quad (13)$$

The median persistence time for each Biome, Realm, and land cover  $\widehat{\Delta t}_{B,R,LC}^*$  is the time corresponding to the 50th percentile of  $\widehat{BA}_{B,R,LC}(\Delta t^*)$ , and is computed as in Equation (12).

$$\widehat{\Delta t}_{B,R,LC}^* = \Delta t^* : \left\{ \int_0^{\Delta t^*} \widehat{BA}_{B,R,LC}(\Delta t^*) = 0.5 \right\} \quad (14)$$

## 4. Results

### 4.1. Fire Activity Distribution

Globally, from 2003 to 2016, the MODIS MCD64A1 product detected, on average,  $4.0 \times 10^6$  km<sup>2</sup> of burned area per year:  $0.19 \times 10^6$  km<sup>2</sup> in Forest,  $0.31 \times 10^6$  km<sup>2</sup> in Shrubland,  $3.1 \times 10^6$  km<sup>2</sup> in Grassland & Savanna, and the remaining  $0.40 \times 10^6$  km<sup>2</sup> occurring in croplands and other land covers not considered in this study. The average annual area burned, reported by land cover and biome and the geographic distribution of area burned by land cover and ecoregion are displayed in Figure 7. The full result tables are presented as supplementary online material (Table S1). Out of the 867 ecoregions defined by the TEOW map, 511 ecoregions had more than 250 km<sup>2</sup> of burned area detected in at least one land cover class over the study period, and were considered in the analysis (Section 3.2.1); 300 ecoregions were considered for the Forest land cover class, 135 for Shrubland and 392 for Grassland & Savanna (Figure 7, right column). The majority of the burned area in the

Forest land cover was detected in the Tropical (65.9%), Boreal (19.1%) and Temperate (13.8%) biomes. The majority of the burned area in Shrubland was detected in the Desert/Xeric (50.0%) and Tropical (41.6%). The majority of the burned area in Grasslands & Savannas was detected in the Tropical (93.4%) and Temperate (3.9%) biomes (Figure 7, left column).

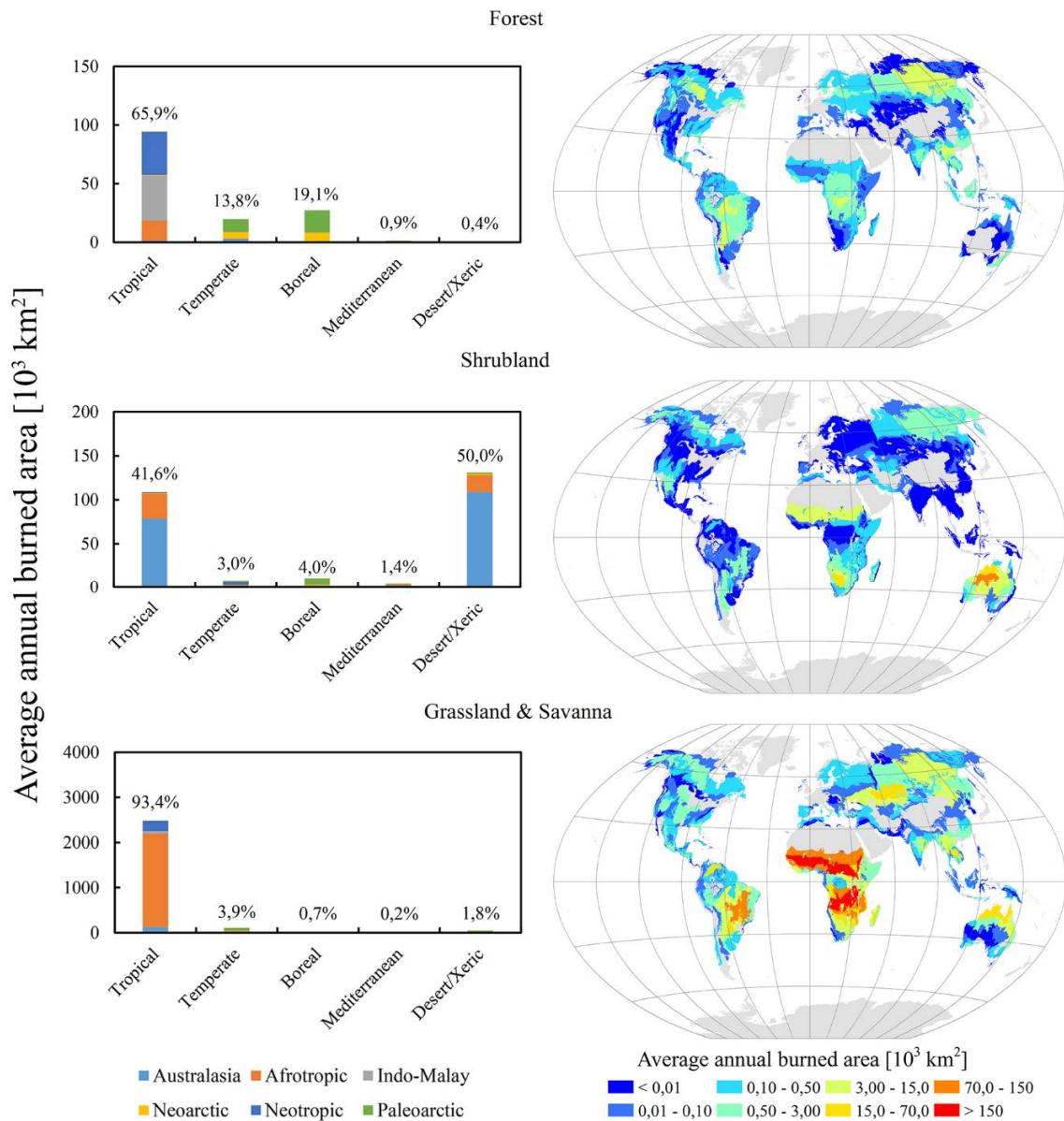


**Figure 7.** Global burned area distribution, as detected by the MODIS global burned area product (MCD64A1) in the 2003–2016 period, stratified by aggregated land cover class. **Left:** histogram of the partition of the average annual burned area by biome and realm. **Right:** average annual burned area detected in each ecoregion. The ecoregions not considered in the analysis because of negligible fire activity are displayed in grey.

The duration of the fire season was calculated in each ecoregion, as described in Section 3.2.1. (Table S2). Figure 8 shows the global distribution of the fire season duration at the ecoregion level. The median duration of the fire season of the ecoregions considered was 112 days (7 × 16-day periods), the shortest 32 days (2 periods) and the longest 304 days (19 periods).

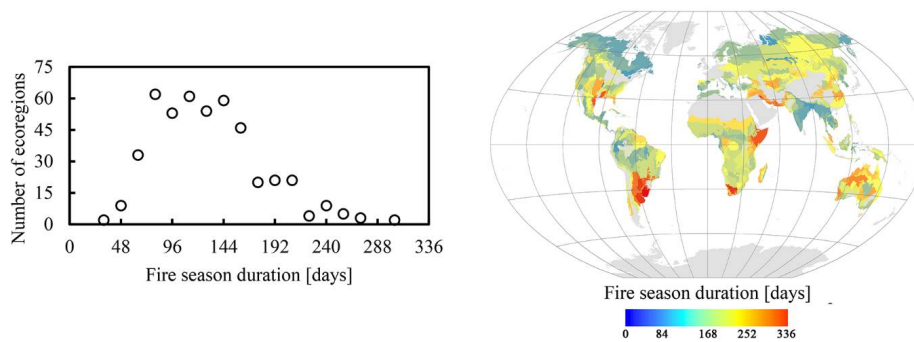


**Figure 8.** Histogram (Left) and map (Right) of the fire season duration, computed for the ecoregions considered in the analysis. The ecoregions not considered in the analysis because of negligible fire activity are displayed in grey.

#### 4.2. Ecoregion Level Burned Area Persistence Time

The burned area persistence time  $\Delta t_{Eco,LC,t}^*$  for each ecoregion (*Eco*), land cover class (*LC*) and 16-day period (*t*) of the fire season (Table S3), as well as the summary metrics  $\hat{BA}_{Eco,LC}(\Delta t^*)$  and  $\hat{\Delta t}_{Eco,LC}^*$  (Table S4) were estimated following the methodology described in Section 3.2.3. The median persistence time  $\hat{\Delta t}_{Eco,LC}^*$  in each ecoregion and land cover, and the corresponding interquartile ranges, are displayed Figure 9.

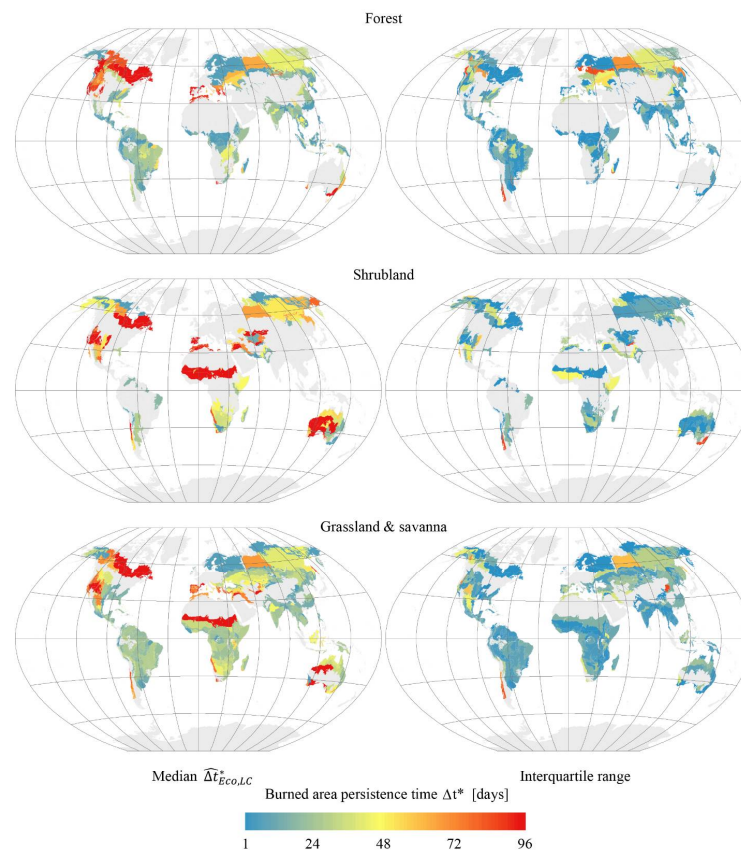


**Figure 9.** Burned area persistence time calculated for each ecoregion, stratified by aggregated land cover class: Forest (top row), Shrubland (middle row), and Grassland & Savanna (bottom row). The median persistence time  $\hat{\Delta t}_{Eco,LC}^*$  (left column) and interquartile range (right column) are shown using a rainbow color scale; the ecoregions not considered in the analysis because of negligible fire activity are displayed in grey.

In Forest, 101 ecoregions (34%), 195 ecoregions (66%), and 230 ecoregions (77%) had a median persistence time shorter than 16, 32, and 48 days, respectively (Figure 10, orange bars). Figure 9, top row, shows that the ecoregions with the shortest median persistence times are generally in the tropics, and those with the longest persistence times are in North America, the Western Mediterranean, and South Eastern Australia. The ecoregions with the highest interquartile range, which represents the persistence time variability during the fire season, are mostly located in Eurasia.

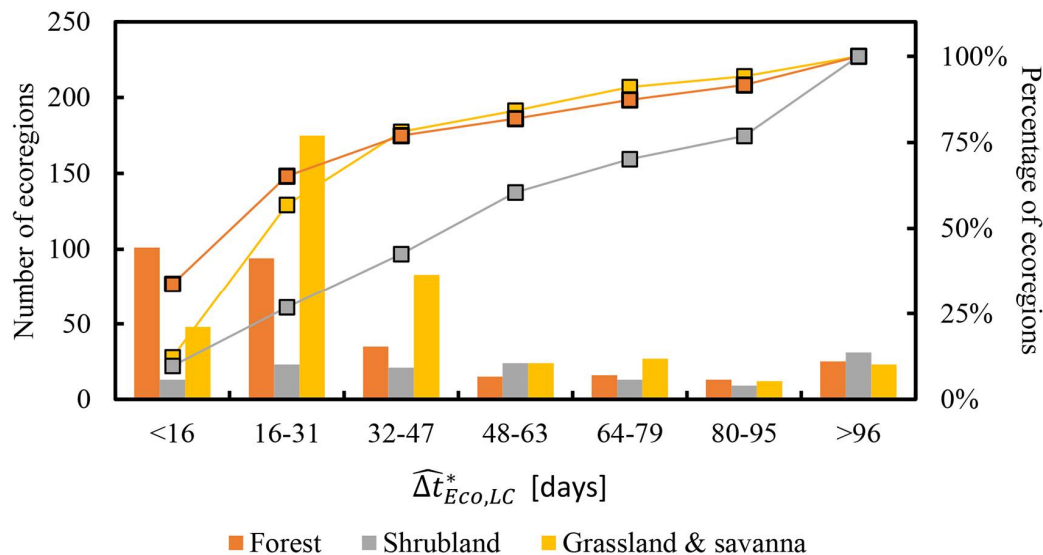


**Figure 10.** Histogram bars and cumulative lines of the estimated persistence time  $\hat{\Delta}t_{Eco,LC}^*$  calculated for all the ecoregions and stratified by aggregated land cover class. The histograms were computed using 16-day bins, up to 96 days after the date of burn.

In Shrubland, only 13 (10%), 36 (27%) and 57 (42%) ecoregions had a median persistence time of under 16, 32, and 48 days respectively, whereas 31 ecoregions (23%) had a persistence time greater or equal than 96 days (Figure 10, gray bars). Figure 9, middle row, shows that the ecoregions with the shortest median persistence time are located in boreal regions, Southern Africa and South America. The longest persistence times correspond to the sub-Saharan and Mediterranean ecoregions, North America, and Western and Central Australia.

Finally, in Grassland & Savanna, 48 (12%), 223 (57%) and 306 (78%) ecoregions had a median persistence time of under 16, 32, and 48 days, respectively (Figure 10, yellow bars). Figure 9, bottom row, shows that the ecoregions with the shortest median persistence time are located in Boreal regions and South-East Asia; those with the longest persistence time are located in North Africa, North America and some regions in central Australia. For this land cover, the great majority of the burned area was detected in the tropical ecoregions of Africa, South America and Australia (Figure 7, bottom row). All these ecoregions, with few exceptions, have a median persistence time between 16 and 48 days, with small variability (interquartile range) (Figure 9, bottom row).

#### 4.3. Biome/Realm Aggregation of the Burned Area Persistence Time

The ecoregion-level results were aggregated into summary metrics for each land cover and Realm/Biome spatial unit, applying the methods described in Section 3.2.4 (Table S5). These results are presented in the following section, which is organized by land cover class.

##### 4.3.1. Forest Land Cover

Forests are among the largest carbon pools of the globe [98], and forest fires are one of the main carbon sources for the atmosphere, contributing to 24.8% of the total global carbon emission from

fires [24], even though forests contribute to just 4.75% ( $0.19 \times 10^6 \text{ km}^2$ ) of the MODIS global annual area burned. Of this area, the majority was detected in Tropical (65.9%), Temperate (13.8%) and Boreal (19.1%) biomes, with a negligible contribution of the other biomes (Figure 7, top left). Although from an ecological perspective, fire effects persist for decades in most forests, the separability of the spectral signature of burned and unburned areas declines quickly. The global distribution of  $\hat{B}A_{B,R,LC}(\Delta t^*)$  (including all the 5 aggregated biomes) (Figure 11, bottom right) indicated that 66.4% of the annual burned area ( $0.09 \times 10^6 \text{ km}^2$  per year) had a persistence time of less than 32 days, and less than 48 days for 79.4% of the annual burned area ( $0.10 \times 10^6 \text{ km}^2$  per year); only 7.2% had a persistence time greater than 96 days. The biome-level distribution of  $\hat{B}A_{B,R,LC}(\Delta t^*)$  is also displayed in Figure 11 and is complemented by the corresponding box plots reporting the median time  $\hat{\Delta}t_{B,R,LC}^*$  and interquartile range (Figure 12). In Tropical biomes, the distribution of  $\hat{B}A_{B,R,LC}(\Delta t^*)$  was unimodal, with short persistence times (80.5% of the area has a persistence under 32 days). In Temperate biomes, the distribution was largely bimodal: the first mode is largely due to burned areas detected in the Paleoarctic realm (where 28.0% of the area has a persistence of less than 16 days); the second mode, at  $\Delta t^* \geq 96$  days, was mainly due to burned area detected in Australasia and Neoarctic realm. In boreal biomes, the distribution is trimodal, due to different behavior in the Neoarctic and Paleoarctic realms. The Paleoarctic realm was characterized by a shorter persistence time ( $\hat{\Delta}t_{B,R,LC}^*$  is 44 days) and bimodal distribution, with a first peak at  $\Delta t^* < 16$  and a second peak at  $48 \leq \Delta t^* < 64$ . The Neoarctic had a longer persistence time ( $\hat{\Delta}t_{B,R,LC}^*$  is  $>96$  days) and unimodal distribution. As a result, the global distribution of  $\hat{B}A_{B,R,LC}(\Delta t^*)$  (Figure 11, bottom right) was a combination of short persistences, mainly from Tropical and Paleoarctic Temperate and Boreal burned areas, and long persistences, mainly from Australasia Temperate and Neoarctic Temperate and Boreal burned areas.

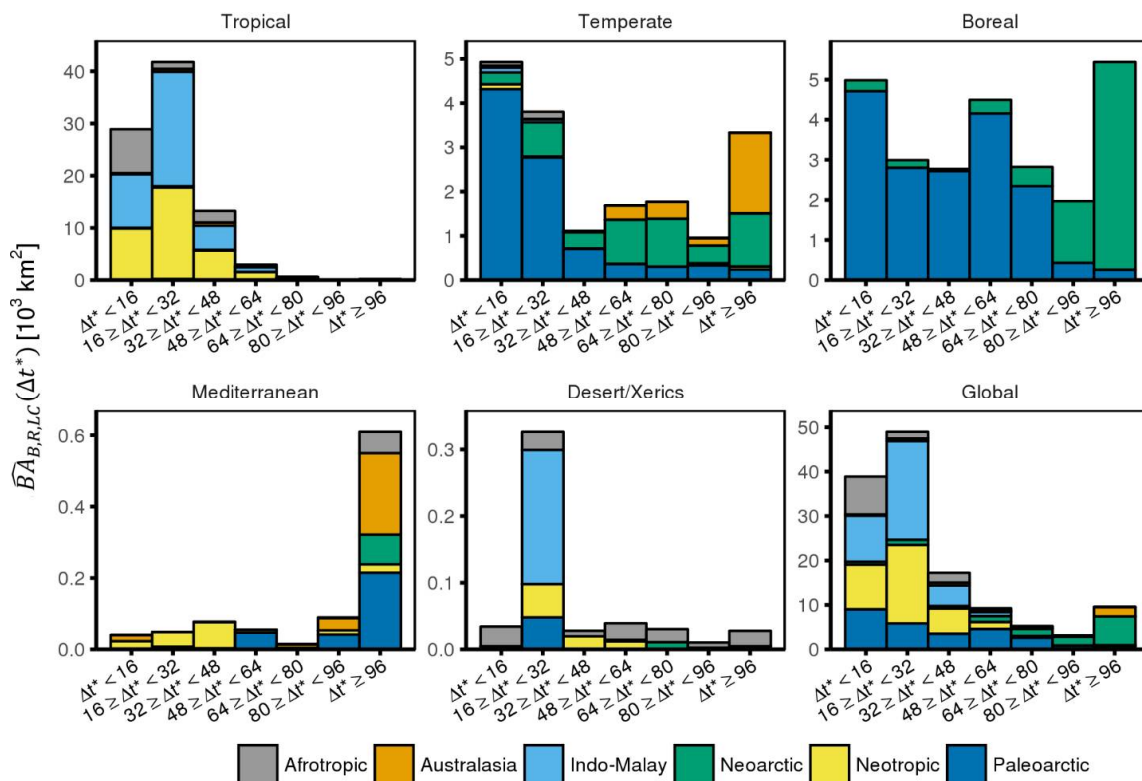


**Figure 11.** Histograms of  $\hat{B}A_{B,R,LC}(\Delta t^*)$  in the Forest aggregated land cover class, presented for each aggregated biome and globally. The colors represent, in each bar of the histograms, the stratification by realm.

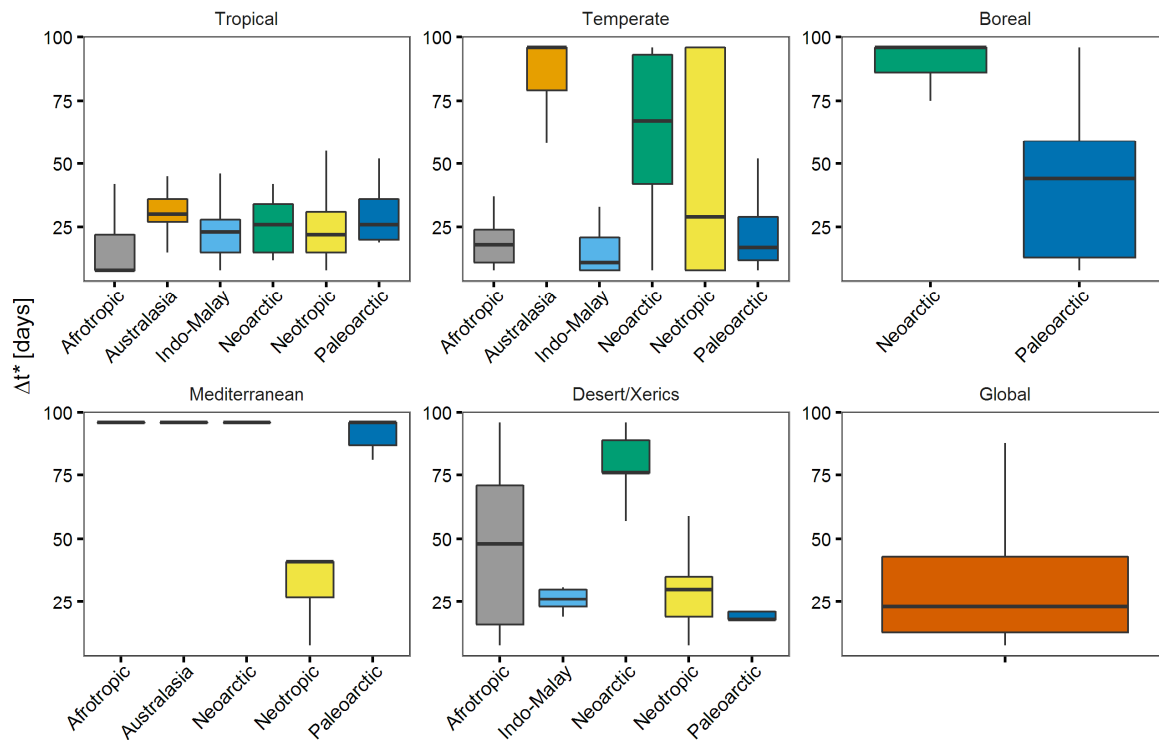


**Figure 12.** Boxplots of  $\hat{B}A_{B,R,LC}(\Delta t^*)$  in the Forest aggregated land cover, organized by aggregated biome and globally. The boxplots show the median (i.e.,  $\hat{\Delta}t_{B,R,LC}^*$ ), interquartile range, minimum and maximum of the distribution.

#### 4.3.2. Shrubland Land Cover

The vast majority of the burned area in the Shrubland aggregated land cover class occurred in the Australasia (73.1%) and Afrotropic (18.7%) realms. In particular, it was a very significant class in the Australasian realm, where it contributed to 46.7% of the average annual burned area. The area burned was almost evenly split between the Tropical (41.6%) and Desert/Xeric (50.0%) biomes, with a negligible contribution of the other biomes (Figure 7, center left). Different persistence times were found in different biomes: shorter in the Tropical biomes, where the mode of the  $\hat{B}A_{B,R,LC}(\Delta t^*)$  histogram was between 16 and 32 days; and longer in the Desert/Xeric biomes, where the mode was greater than 96 days (Figures 13 and 14). The global histogram is bimodal, and reflects the distinct distribution of these two dominant biomes (Figure 13).

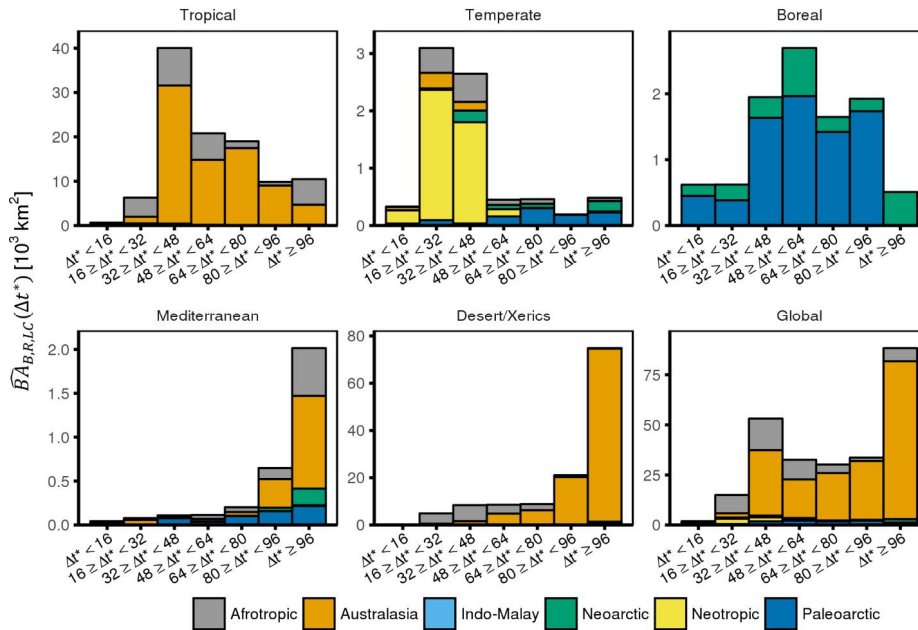


**Figure 13.** Histograms of  $\hat{B}A_{B,R,LC}(\Delta t^*)$  in the Shrubland aggregated land cover class, presented for each aggregated biome and globally. The colors represent, in each bar of the histograms, the stratification by realm.

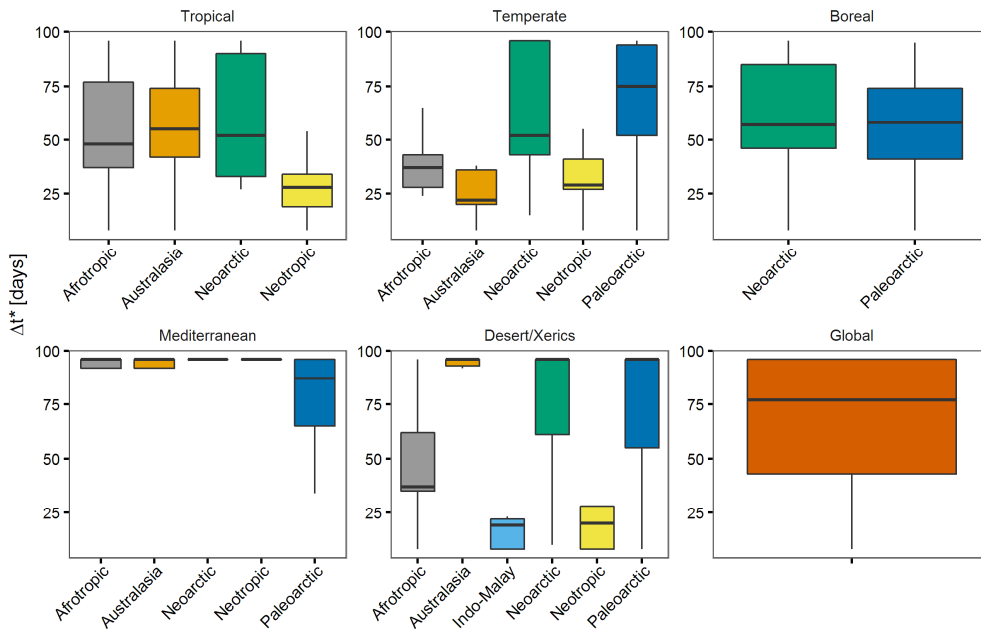


**Figure 14.** Boxplots of  $\hat{B}A_{B,R,LC}(\Delta t^*)$  in the Shrubland aggregated land cover, organized by aggregated biome and globally. The boxplots show the median (i.e.,  $\hat{\Delta t}_{B,R,LC}^*$ ), interquartile range, minimum and maximum of the distribution.

### 4.3.3. Grassland & Savanna Land Cover

The vast majority (93.4%) of the burned area for Grassland & Savanna was detected in the Tropical biome. Only 3.9% was detected in the Temperate biome, with a negligible contribution of the other biomes (Figure 7, bottom row). In particular, the majority of the global burned area detections were concentrated in the Tropical biome of the Afrotropic realm (76%). Globally, the mode of the  $\hat{B}A_{B,R,LC}(\Delta t^*)$  histogram (Figure 15, bottom right) was between 16 and 32 days (60.5% of the annual

burned area). Overall, the persistence time was short: 91% of the area burned had a persistence time of between 16 and 48 days, resulting in a median estimated time  $\hat{\Delta}t^*$  of 29 days (Figures 15 and 16). At biome level, the histograms of  $\hat{B}A_{B,R,LC}(\Delta t^*)$  for Tropical and Temperate biomes were both unimodal. The histogram of  $\hat{B}A_{B,R,LC}(\Delta t^*)$  had its maximum between 16 and 32 days for Tropical biomes and between 32 and 48 days for Temperate biomes. A total of 92.7% of  $\hat{B}A_{B,R,LC}(\Delta t^*)$  for Tropical biomes and 80.5% for Temperate biomes was associated to  $\Delta t^*$  between 16 and 48 days. The global histogram was unimodal, and reflects the distribution of the dominant Tropical biomes and a small contribution from the Temperate biomes (Figure 15).

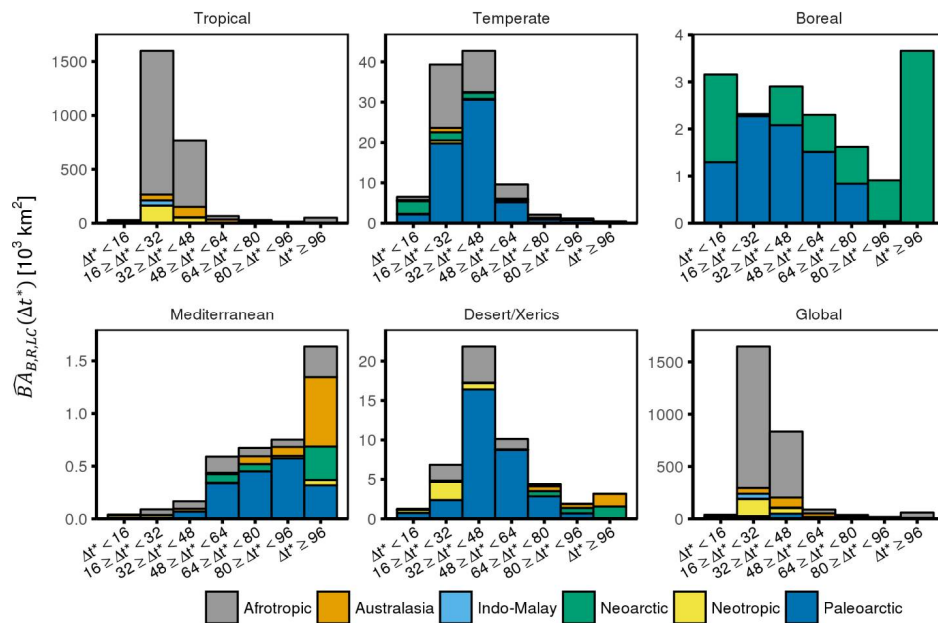


**Figure 15.** Histograms of  $\hat{B}A_{B,R,LC}(\Delta t^*)$  in the Grassland & Savanna aggregated land cover class, presented for each aggregated biome and globally. The colors represent, in each bar of the histograms, the stratification by realm.

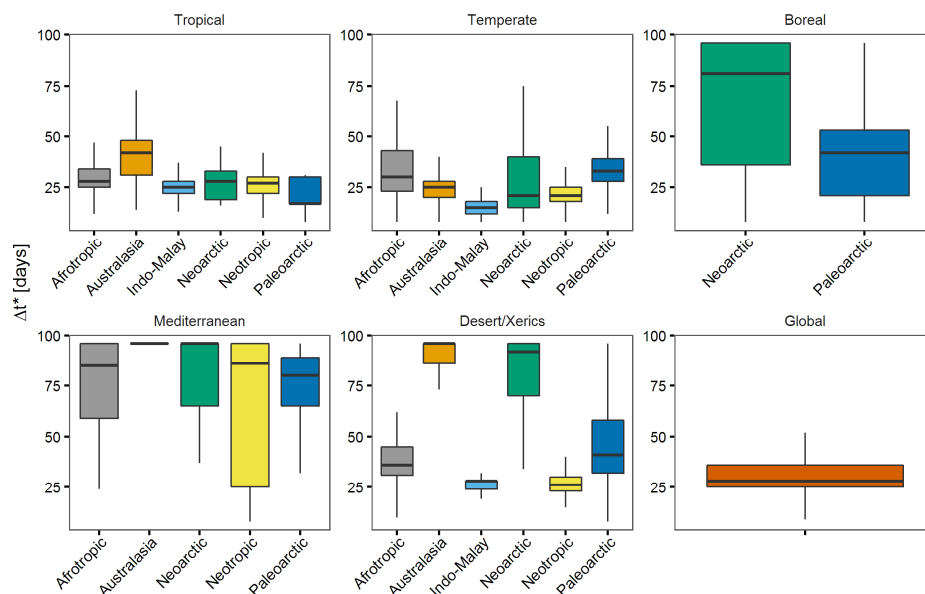


**Figure 16.** Boxplots of  $\hat{B}A_{B,R,LC}(\Delta t^*)$  in the Grassland & Savanna aggregated land cover, organized by aggregated biome and globally. The boxplots show the median (i.e.,  $\hat{\Delta}t_{B,R,LC}^*$ ), interquartile range, minimum and maximum of the distribution.

## 5. Discussion

### 5.1. Ecoregion-Level Burned Area Persistence Time

The results at ecoregion level confirmed that the separability of burned and unburned surfaces quickly decreases after burning, even in ecosystems where the fire effects on the vegetation are persistent for several years. In addition to the dissipation of the charcoal and ashes, vegetation regrowth in burned areas, phenology of unburned vegetation, and several other factors might have contributed to these results.

In this study, the post-fire spectral temporal variations were analyzed by using NBR time series of burned and unburned pixels, as identified by the MCD64A1 global burned area product. Detection errors in the MCD64A1 product influenced the results, by reducing the separability of the burned (Equation (4)) and unburned (Equation (5)) probability distributions. More specifically, omission errors resulted in the inclusion of burned pixels in the unburned population  $ub$ , and biased positively the function  $F_{UB}$  (Equation (7)). Conversely, commission errors caused the inclusion of unburned pixels in the burned population  $ba$ , biasing negatively the function  $F_B$  (Equation (6)). As a result, both omission and commission errors in the MCD64A1 product resulted in a shorter estimated persistence time (Equation (8)).

Furthermore, the maximum persistence time  $\Delta t^*_{jday}$  (Equation (8)) is limited by the length of the post-fire time series of nadir BRDF-adjusted reflectances (MCD43A4). Because at least 7 cloud-free MODIS observations within a 16-day period are needed to perform a valid BRDF inversion [52], in regions with clearly defined dry and wet seasons, or with persistent snow cover in the winter months, no MCD64A4 data were available for part of the year. If the fire season was close to the beginning of the wet or snow season, the estimated persistence time was effectively limited to the duration of the cloud-free period.

Cropland land cover was not considered in our analysis, since the MODIS burned area product is not suited to capturing the size and heterogeneity of cropland burned areas [18,99] because of its geometrical resolution, and because other agricultural practices (e.g., tilling) often immediately follow the fires [100], and have similar spectral signatures [101]. Omission errors in the cropland class of the MCD12Q1 land cover product, therefore, led to the inclusion of MCD64A1 detections over agricultural areas in the burned population  $ba$ . Some of these were genuine detections, but had a very short persistence time; some were commission errors and—as detailed above—negatively biased the  $F_B$  function; in either case, the result was an underestimation of the persistence time. Additional errors in the MCD12 land cover map also influenced the estimated persistence time, by reducing the effectiveness of the stratification by aggregated land cover type.

Finally, caution should be used in considering the estimated burned area persistence time as defined in the present work; it should not be confused with the ecological concept of vegetation recovery to pre-fire level [102–104]. The duration of the persistence time can be limited by the recovery of NBR values to pre-fire levels after rapid re-vegetation or other factors, such as snowfall, that occlude the charcoal and bare soil and mask the spectral signature associated with burned areas. Additionally, errors in the MODIS burned area and land cover product could have influenced the stratification of the analysis and the division in the two population of burned and unburned pixels reducing the estimated persistence time.

### 5.2. Biome/Realm Level Burned Area Persistence Time

#### 5.2.1. Forest Land Cover

The majority of the burned area in Tropical biomes was detected in the Afrotropic, Indo-Malay and Neotropical realms (Figure 7, top left). In these three realms, the median persistence time  $\hat{\Delta}t^*_{B,R,LC}$  was 8, 24 and 26 days, respectively (Figures 11 and 12, top left). Compared to the other biomes, tropical forests had shorter persistence times, arguably due to several factors. Many tropical forests have

dense canopies that keep surface fuels moist and humidity high, limiting fire spread and duration, and allowing vegetation to recover quickly [105]. New photosynthetically active vegetation can alter the post-fire spectral signature sensed by EO satellites and deteriorate their ability to detect burned areas. For example, after a tropical forest fire in the Congo Basin, a new surface layer of vegetation established (*Marantaceae*), which covered the burned area in less than 3 months after the burning event [106].

Additionally, the estimated persistence time was influenced by the nature of tropical forest fires. Anthropogenic activities account for the majority of burning events in the tropical Amazon rainforest [107,108], African rainforests [89,109,110] and Indo-Australian rainforests [111]. In central Africa, human-ignited rainforest fires are strongly associated with land cover changes and are influenced by fire activity along the edges of the forest [89]. In Amazonia, fire activity is connected to other disturbances that have spectral similarities with burned areas, such as logging and deforestation, that only complex algorithms can discriminate [112]. In both of these cases, post-fire NBR may recover rapidly in areas planted immediately after clearing, where vegetation regrows within weeks [105]. In Southern China, various forest fire regimes were found [113]; regions characterized by long fire seasons and frequent fires, mainly due to human activity, show lower estimates of persistence time compared to regions characterized by shorter fire season and infrequent fires.

The majority of the burned area in Temperate biomes was detected in Australasia, Neartic and Neotropic realms (Figure 7, top left). In these three realms, the median persistence time  $\hat{\Delta}t_{B,R,LC}^*$  was >96, 67 and 29 days, respectively (Figures 11 and 12, top center). In Australasia, these results were consistent with the occurrence of high-intensity, low-frequency fires in dense, shade-tolerant understory vegetation in many temperate forests in Australia [84,114]. For the Neartic realm temperate forests, the median persistence time  $\hat{\Delta}t_{B,R,LC}^*$  was the result of variable  $\hat{\Delta}t_{Eco,LC}^*$  at the ecoregion level. The longest persistence time estimates occurred in mid-elevation, Northern Rockies ecoregions typically affected by large crown fires [115,116]. The shortest persistence times were in the southeast US, which is consistent with frequent surface fires and rapid post-fire grass regeneration observed in that region [117,118].  $\hat{\Delta}t_{B,R,LC}^*$  estimated for the Paleartic realm temperate forests was greatly influenced by the presence of anthropogenic fires linked to land conversion for roads and croplands in the western China and Russia-China borders regions [119], in which the MODIS MCD64A1 product detects the majority of burned areas for this combination of realm and realm (Figure 7, top right).

The Boreal biome is present only in the Neartic and Paleartic realms, accounting for 29.9% and 70.1% percent of the annual burned area respectively (Figure 7, top left). The estimated median persistence time  $\hat{\Delta}t_{B,R,LC}^*$  was 44 days in the Paleartic realm, and >96 days in the Neartic (Figures 11 and 12, top right). This large difference was likely due to the different burning conditions in these two realms. Fires in Paleartic boreal forests are dominated by low-intensity surface fires, and typically result in smaller-sized fires than Neartic boreal forests fires, where high-intensity crown fires are instead predominant [120,121]. Furthermore, the fire temporal distribution in the Paleartic realm was consistent with anthropogenic agricultural fires that typically occur in spring and fall and clear extensive areas of surface fuels [100,121]. The size and timing of Paleartic fire reduced the spectral separability of burned/unburned pixels in boreal biomes because of limited data quality (e.g., mixed pixels resulting from land-snow patterns and vegetation phenology) and availability (e.g., spatial resolution, cloud-free data availability) [46]. For the Boreal biomes, fire season is often followed closely by the snow season. As discussed in Section 4.2, the estimated persistence time was influenced by missing data due to snow cover, especially when the majority of burned areas were detected at the end of the fire season, such as in the Paleartic Boreal realm.

### 5.2.2. Shrubland Land Cover

The median persistence time  $\hat{\Delta}t_{B,R,LC}^*$  for the Australasia realm was 55 days for the Tropical biome and >96 days for the Desert/Xeric biome. Tropical fires in Shrubland land cover are typically

characterized by a shorter persistence of char on the ground due to removal by wind and atmospheric agents; the observability is also limited by cloud cover immediately following the fire season [45]. For example, Bowman, Zhang, Walsh and Williams [44] found the temporal persistence of the burned areas in tropical regions of the Australian northern territories to be less than 100 days. Conversely, fire scars in arid zones are typically more persistent, as—once the charcoals and ash have dissipated—there is little vegetation regrowth until the wet season, leading to persistent soil exposure. The NBR value of soil is significantly different from unburned vegetation [122], leading to a longer estimated persistence time.

The median persistence time  $\hat{\Delta}t_{B,R,LC}^*$  in the Afrotropic realm was 48 days and 37 days for the Tropical and the Desert/Xeric biomes, respectively. In both biomes, the persistence time had a large variability, with interquartile ranges of 37–77 days and 35–62 days (Figure 14, grey boxplot of Tropical and Desert/Xeric plots). Tropical shrubland fires are concentrated in the Sahelian zone in North equatorial Africa, including areas in East Africa, and the Kalahari region in South equatorial Africa [123]. In the central Kalahari, the majority of fire events can interest only herbaceous vegetation, while woody fuels remain unburned; only higher-intensity fires are able to burn even in the woody-cover dominated areas [124]. The NBR time series over burned areas showed variable changes in magnitude depending on the amount of unscorched vegetation within a MODIS pixel, and, as a result, the persistence time duration was variable. Finally, the persistence time large variability is potentially due to the different anthropogenic influence of fire activity over managed and protected land [125].

### 5.2.3. Grassland & Savanna Land Cover

Grasslands and savannas are fire-prone ecosystems, and fire is an essential factor contributing to the maintenance of the ecosystem; where resource availability and climatic control would allow tree seedling establishment, fire decreases tree cover density and maintains grassland and savanna ecosystems [8,126,127]. The short estimate and the small variability of the burned area persistence time for this land cover (Figure 16, bottom right) could be explained by the common features that grassland and savanna share across the continents. Fine fuels and low fuel loadings result in a shorter persistence of the char residue signal; cloud cover and the frequent presence of extensive smoke aerosol layers result in a limited availability of satellite optical data, and the dominance of surface fires exacerbate the problem of detecting burns in woody savannas [45].

The majority of the burned area in Tropical biomes was detected in the Afrotropic, Australasia and Neotropic realms (Figure 7, bottom left). In these three realms, the median persistence time  $\hat{\Delta}t_{B,R,LC}^*$  was 28, 42 and 27 days, respectively (Figures 15 and 16, top left). In the tropics and subtropics, the total amount of burned area and the interannual variability are controlled by the complex interaction between climate, fuel, and human activity [5,16,128]. The spectral characteristics of vegetation and burned areas change depending on the acquisition date [129] and are highly dynamic; rapid re-vegetation after a fire and the presence of unburned fuel loads can significantly impact the spectral signal [37,45].

The persistence time for Grasslands & Savanna was in accordance with other studies in tropical savannas. Scholes and Walker [130] reported a recovery to pre-fire albedo values 42 days after a fire in a southern African savanna. Likewise, ground-based reflectance was observed to be within 20% of pre-fire values within 14 days of burning events in western African savannas [41,42]. Eva and Lambin [131] analyzed the spectral reflectance temporal dynamics of burned and unburned woodland savannas in Central Africa using ATSR data and concluded that the discrimination between burned and unburned areas was affected by an error of 20% after 35 days from the fire event. The majority of the burned area persistence time for Tropical Australasia realm was longer than the Afrotropic realm (Figure 16, top left). This difference was likely caused by the different dominant fire regimes of the two realms. In both realms, savanna fire frequency is annual/biannual; Australia has larger, more intense fires, whereas Africa is characterized by smaller, less intense fires [84]. Australian tropical savanna

fire intensity rises as the dry season progresses due to more extreme fire weather and fire-prone fuel conditions in the later season [132–134]. A variable degree of change in the spectral signal caused by the action of fire was reported in Tropical grasslands and savannas [129], which is consistent with the variability of Grassland & Savanna persistence time results over Afrotropic and Australasian Tropical biomes (Figure 16, top left).

The majority of the burned area in Temperate biomes was detected in the Afrotropic, Neoarctic, and Paleoarctic realms (Figure 7, bottom left). In these three realms, the median persistence time  $\hat{\Delta}t_{B,R,LC}^*$  was respectively 30, 21 and 33 days (Figures 15 and 16, top center). Like other biomes, Grassland & Savanna fire activity in temperate biomes is mainly driven by climate and human activity. In North American temperate grassland ecoregions, antecedent precipitation amount and the drought index significantly influence fire activity as high-precipitation years can increase fuel load and subsequent fire intensity in the drought years that follow [135].

Agricultural fires detected in the MODIS land cover product were discarded in this work. Nevertheless, misclassified crop, managed prairie and pasture fires were likely included in the analysis and could reduce the estimated burned area persistence time, especially in ecoregions of the Paleoarctic realm where the use of fire is widespread as an agricultural management tool for the removal of excess residue and the control of diseases and pests [136]. Typically, temperate grasslands are intensively managed, including fire and grazing practices that alter nutrient cycling and the distribution of organic matter [127,137]. The relatively short burned area persistence time for temperate grassland was also observed in Canadian grassland fires. In these grasslands, Lu and He [138] estimated the post-fire vegetation recovery using multi-temporal Landsat imagery (one, two and three months after the fire) and concluded that grassland has a strong post-fire recovery capacity, especially if there is an adequate water availability. Prescribed fires are commonly used in tallgrass prairie ecosystems and are characterized by a relatively small-sized high degree of combustion heterogeneity, for this reason, MODIS' coarse resolution could be insufficient for an adequate mapping of this type of fire [139].

## 6. Conclusions

Coarse-resolution sensors typically have a daily temporal resolution, and it is generally assumed that a sufficient number of observations will be available for mapping burned areas globally. However, moderate-resolution satellites have reduced temporal resolutions (e.g., 16 days for Landsat, 5 days for Sentinel-2A/B), which could potentially lead to large burned area omission errors in ecosystems where the spectral signal associated with burning disappears quickly, especially if more than one post-fire observation is required to detect the burn. This paper attempted to calculate the burned area persistence time to estimate the period of time after the burn date in which burned areas are detectable using remotely sensed data change detection.

The presented methodology estimated the burned area persistence time defined as the duration of the spectral separability of burned/unburned areas, using time series of Normalized Burn Ratio (NBR) spectral index computed from MCD43A4 BRDF-adjusted MODIS reflectances. Burned and unburned areas were defined based on the MCD64A1 MODIS global burned area product. The full global MODIS record for the years 2003–2016 was used.

Among the novel aspects of the proposed methods, a probabilistic method for the analysis of spectral separability over time and space was developed, which can be extended to the analysis of other disturbances and, in general, of other non-permanent land use or land cover changes. The methods were stratified spatially (ecoregion and land cover) and temporally (time of the year) and provided for a rigorous generalization at coarser units.

The results showed that the persistence time was highly variable in time and space. Not only was it different across land cover classes, but within the same class, it depended on biome and realm. The shortest burned area persistence times were found over Tropical Forests, confirming that the separability of burned and unburned surfaces quickly decreases after burning, even in ecosystems where the fire effects on the vegetation are persistent for several years. The persistence times in Tropical

forests were mostly limited by the rapid surface vegetation regrowth and the influence on the spectral signal of unscorched canopies. The longest persistence times were found in Desert/Xeric Shrublands, which are characterized by little vegetation regrowth until the wet season, leading to persistent soil exposure spectrally different from the unburned. Burned area persistence times over Grassland & Savanna, mostly detected on the African continent, were short and with small variability (16–48 days) due to the fine fuels and fuel loadings typical of savanna fires.

Ultimately, the results indicated that, globally, burned areas can be detected for a limited time by optical satellite sensors; globally, the median burned area persistence time was estimated to be 29 days, and 86.6% of the area detected as burned in the MODIS MCD64A1 product can be mapped accurately for a maximum of only 48 days. Thus, results indicate that burned area persistence time can be a limiting factor for global burned area mapping from moderate resolution satellite sensors, which have a low temporal resolution. Future research is suggested to investigate the effect of cloud cover, which further limits the burned area mapping capability of moderate-resolution sensors for the majority of burned areas, which can be detected reliably only for a relatively short time.

**Supplementary Materials:** The following are available online at <http://www.mdpi.com/2072-4292/10/5/750/s1>, Table S1: Ecoregion MODIS burned area 2003–2016, Table S2: Ecoregion fire season, Table S3: Ecoregion burned area persistence time, Table S4: Ecoregion summary metrics, Table S5: Spatial unit Biome/Realm summary metrics.

**Author Contributions:** A.M. and L.B. conceived the experiments; A.M. developed the code and processed the data and developed the graphics with assistance from L.B.; and A.M. structured and drafted the manuscript with assistance from L.B.

**Acknowledgments:** The authors would like to thank David Roy, Andrew Hudak and Lee Vierling for their helpful comments and suggestions. This research was funded by the NASA Earth and Space Science Fellowship Grant NNX16AO11H and by NASA Land Cover/Land Use Change (LCLUC14-2), Multi-Source Land Imaging Science Program, Grant NNX15AK94G.

**Conflicts of Interest:** The authors declare no conflict of interest.

## References

1. DeBano, L.F.; Neary, D.G.; Ffolliott, P.F. *Fire Effects on Ecosystems*; John Wiley & Sons Incorporated: Hoboken, NJ, USA, 1998.
2. Bowman, D.M.; Balch, J.K.; Artaxo, P.; Bond, W.J.; Carlson, J.M.; Cochrane, M.A.; D'Antonio, C.M.; DeFries, R.S.; Doyle, J.C.; Harrison, S.P. Fire in the earth system. *Science* **2009**, *324*, 481–484. [[CrossRef](#)] [[PubMed](#)]
3. Certini, G. Effects of fire on properties of forest soils: A review. *Oecologia* **2005**, *143*, 1–10. [[CrossRef](#)] [[PubMed](#)]
4. Van der Werf, G.R.; Randerson, J.T.; Giglio, L.; Collatz, G.; Mu, M.; Kasibhatla, P.S.; Morton, D.C.; DeFries, R.; Jin, Y.V.; van Leeuwen, T.T. Global fire emissions and the contribution of deforestation, savanna, forest, agricultural, and peat fires (1997–2009). *Atmos. Chem. Phys.* **2010**, *10*, 11707–11735. [[CrossRef](#)]
5. Van der Werf, G.R.; Randerson, J.T.; Giglio, L.; Collatz, G.J.; Kasibhatla, P.S.; Arellano, A.F., Jr. Interannual variability in global biomass burning emissions from 1997 to 2004. *Atmos. Chem. Phys.* **2006**, *6*, 3423–3441. [[CrossRef](#)]
6. Thonicke, K.; Venevsky, S.; Sitch, S.; Cramer, W. The role of fire disturbance for global vegetation dynamics: Coupling fire into a dynamic global vegetation model. *Glob. Ecol. Biogeogr.* **2001**, *10*, 661–677. [[CrossRef](#)]
7. Goetz, S.J.; Bond-Lamberty, B.; Law, B.E.; Hicke, J.A.; Huang, C.; Houghton, R.A.; McNulty, S.; O'Halloran, T.; Harmon, M.; Meddens, A.J.H.; et al. Observations and assessment of forest carbon dynamics following disturbance in North America. *J. Geophys. Res. Biogeosci.* **2012**, *117*. [[CrossRef](#)]
8. Bond, W.; Woodward, F.; Midgley, G. The global distribution of ecosystems in a world without fire. *New Phytol.* **2005**, *165*, 525–538. [[CrossRef](#)] [[PubMed](#)]
9. Jin, Y.; Roy, D. Fire-induced albedo change and its radiative forcing at the surface in northern Australia. *Geophys. Res. Lett.* **2005**, *32*. [[CrossRef](#)]

10. Randerson, J.T.; Liu, H.; Flanner, M.G.; Chambers, S.D.; Jin, Y.; Hess, P.G.; Pfister, G.; Mack, M.C.; Treseder, K.K.; Welp, L.R.; et al. The impact of boreal forest fire on climate warming. *Science* **2006**, *314*, 1130–1132. [[CrossRef](#)] [[PubMed](#)]
11. Pfeifer, M.; Disney, M.; Quaife, T.; Marchant, R. Terrestrial ecosystems from space: A review of earth observation products for macroecology applications. *Glob. Ecol. Biogeogr.* **2012**, *21*, 603–624. [[CrossRef](#)]
12. Langmann, B.; Duncan, B.; Textor, C.; Trentmann, J.; van der Werf, G.R. Vegetation fire emissions and their impact on air pollution and climate. *Atmos. Environ.* **2009**, *43*, 107–116. [[CrossRef](#)]
13. Jin, Y.; Randerson, J.T.; Goulden, M.L.; Goetz, S.J. Post-fire changes in net shortwave radiation along a latitudinal gradient in boreal North America. *Geophys. Res. Lett.* **2012**, *39*. [[CrossRef](#)]
14. Lyons, E.A.; Jin, Y.; Randerson, J.T. Changes in surface albedo after fire in boreal forest ecosystems of interior alaska assessed using MODIS satellite observations. *J. Geophys. Res. Biogeosci.* **2008**, *113*. [[CrossRef](#)]
15. GCOS. *Systematic Observation Requirements for Satellite-Based Products for Climate in Support of the UNFCCC*; WMO GCOS Tech. Doc. GCOS-138 WMO-TD 1523; WMO: Geneva, Switzerland, 2011; p. 23.
16. Giglio, L.; Randerson, J.T.; van der Werf, G.R. Analysis of daily, monthly, and annual burned area using the fourth-generation global fire emissions database (GFED4). *J. Geophys. Res. Biogeosci.* **2013**, *118*, 317–328. [[CrossRef](#)]
17. Alonso-Canas, I.; Chuvieco, E. Global burned area mapping from ENVISAT-MERIS and MODIS active fire data. *Remote Sens. Environ.* **2015**, *163*, 140–152. [[CrossRef](#)]
18. Giglio, L.; Loboda, T.; Roy, D.P.; Quayle, B.; Justice, C.O. An active-fire based burned area mapping algorithm for the MODIS sensor. *Remote Sens. Environ.* **2009**, *113*, 408–420. [[CrossRef](#)]
19. Roy, D.; Jin, Y.; Lewis, P.; Justice, C. Prototyping a global algorithm for systematic fire-affected area mapping using MODIS time series data. *Remote Sens. Environ.* **2005**, *97*, 137–162. [[CrossRef](#)]
20. Simon, M.; Plummer, S.; Fierens, F.; Hoelzemann, J.; Arino, O. Burnt area detection at global scale using ATSR-2: The GLOBSCAR products and their qualification. *J. Geophys. Res. Atmos.* **2004**, *109*. [[CrossRef](#)]
21. Tansey, K.; Gregoire, J.M.; Defourny, P.; Leigh, R.; Pekel, J.F.O.; van Bogaert, E.; Bartholome, E. A new, global, multi-annual (2000–2007) burnt area product at 1 km resolution. *Geophys. Res. Lett.* **2008**, *35*. [[CrossRef](#)]
22. Tansey, K.; Grégoire, J.-M.; Stroppiana, D.; Sousa, A.; Silva, J.; Pereira, J.M.C.; Boschetti, L.; Maggi, M.; Brivio, P.A.; Fraser, R.; et al. Vegetation burning in the year 2000: Global burned area estimates from spot vegetation data. *J. Geophys. Res. Atmos.* **2004**, *109*. [[CrossRef](#)]
23. Andela, N.; Morton, D.C.; Giglio, L.; Chen, Y.; van der Werf, G.R.; Kasibhatla, P.S.; DeFries, R.S.; Collatz, G.J.; Hantson, S.; Kloster, S.; et al. A human-driven decline in global burned area. *Science* **2017**, *356*, 1356–1362. [[CrossRef](#)] [[PubMed](#)]
24. Van der Werf, G.R.; Randerson, J.T.; Giglio, L.; van Leeuwen, T.T.; Chen, Y.; Rogers, B.M.; Mu, M.; van Marle, M.J.; Morton, D.C.; Collatz, G.J. Global fire emissions estimates during 1997–2016. *Earth Syst. Sci. Data* **2017**, *9*, 697. [[CrossRef](#)]
25. Kaiser, J.; Heil, A.; Andreae, M.; Benedetti, A.; Chubarova, N.; Jones, L.; Morcrette, J.-J.; Razinger, M.; Schultz, M.; Suttie, M. Biomass burning emissions estimated with a global fire assimilation system based on observed fire radiative power. *Biogeosciences* **2012**, *9*, 527–554. [[CrossRef](#)]
26. Lamarque, J.F.; Bond, T.C.; Eyring, V.; Granier, C.; Heil, A.; Klimont, Z.; Lee, D.; Liousse, C.; Mieville, A.; Owen, B.; et al. Historical (1850–2000) gridded anthropogenic and biomass burning emissions of reactive gases and aerosols: Methodology and application. *Atmos. Chem. Phys.* **2010**, *10*, 7017–7039. [[CrossRef](#)]
27. Tubiello, F.N.; Salvatore, M.; Rossi, S.; Ferrara, A.; Fitton, N.; Smith, P. The FAOSTAT database of greenhouse gas emissions from agriculture. *Environ. Res. Lett.* **2013**, *8*, 015009. [[CrossRef](#)]
28. Rossi, S.; Tubiello, F.N.; Prosperi, P.; Salvatore, M.; Jacobs, H.; Biancalani, R.; House, J.I.; Boschetti, L. FAOSTAT estimates of greenhouse gas emissions from biomass and peat fires. *Clim. Chang.* **2016**, *135*, 699–711. [[CrossRef](#)]
29. Boschetti, L.; Flasse, S.P.; Brivio, P.A. Analysis of the conflict between omission and commission in low spatial resolution dichotomic thematic products: The pareto boundary. *Remote Sens. Environ.* **2004**, *91*, 280–292. [[CrossRef](#)]
30. Randerson, J.T.; Chen, Y.; van der Werf, G.R.; Rogers, B.M.; Morton, D.C. Global burned area and biomass burning emissions from small fires. *J. Geophys. Res. Biogeosci.* **2012**, *117*. [[CrossRef](#)]

31. Mouillot, F.; Schultz, M.G.; Yue, C.; Cadule, P.; Tansey, K.; Ciais, P.; Chuvieco, E. Ten years of global burned area products from spaceborne remote sensing—A review: Analysis of user needs and recommendations for future developments. *Int. J. Appl. Earth Obs. Geoinf.* **2014**, *26*, 64–79. [[CrossRef](#)]
32. Hyer, E.J.; Reid, J.S. Baseline uncertainties in biomass burning emission models resulting from spatial error in satellite active fire location data. *Geophys. Res. Lett.* **2009**, *36*. [[CrossRef](#)]
33. Boschetti, L.; Roy, D.P.; Justice, C.O.; Humber, M.L. Modis–Landsat fusion for large area 30m burned area mapping. *Remote Sens. Environ.* **2015**, *161*, 27–42. [[CrossRef](#)]
34. Roy, D.; Huang, H.; Kumar, S.; Zhang, H.; Li, J.; Gomez-Dans, J.; Lewis, P.; Boschetti, L. Towards prototyping a global Landsat-8 sentinel-2 burned area product. In Proceedings of the EARSEL SIG Fire 2015, Limassol, Cyprus, 2–5 November 2015.
35. Hawbaker, T.J.; Vanderhoof, M.K.; Beal, Y.-J.; Takacs, J.D.; Schmidt, G.L.; Falgout, J.T.; Williams, B.; Fairaux, N.M.; Caldwell, M.K.; Picotte, J.J.; et al. Mapping burned areas using dense time-series of Landsat data. *Remote Sens. Environ.* **2017**, *198*, 504–522. [[CrossRef](#)]
36. Pereira, J.; Chuvieco, E.; Beaudoin, A.; Desbois, N. *Remote Sensing of Burned Areas: A Review*; A review of Remote Sensing Methods for the Study of Large Wildland Fires; Departamento de Geografía, Universidad de Alcalá: Alcalá de Henares, Spain, 1997; pp. 127–184.
37. Trigg, S.; Flasse, S. Characterizing the spectral-temporal response of burned savannah using in situ spectroradiometry and infrared thermometry. *Int. J. Remote Sens.* **2000**, *21*, 3161–3168. [[CrossRef](#)]
38. Fraser, R.H.; Li, Z.; Landry, R. Spot vegetation for characterizing boreal forest fires. *Int. J. Remote Sens.* **2000**, *21*, 3525–3532. [[CrossRef](#)]
39. Chu, T.; Guo, X.; Takeda, K. Remote sensing approach to detect post-fire vegetation regrowth in Siberian boreal larch forest. *Ecol. Ind.* **2016**, *62*, 32–46. [[CrossRef](#)]
40. Solans Vila, J.P.; Barbosa, P. Post-fire vegetation regrowth detection in the Deiva Marina region (Liguria-Italy) using Landsat TM and ETM+ data. *Ecol. Model.* **2010**, *221*, 75–84. [[CrossRef](#)]
41. Frederiksen, P.; Langaas, S.; Mbaye, M. NOAA-AVHRR and GIS-based monitoring of fire activity in Senegal—A provisional methodology and potential applications. In *Fire in the Tropical Biota*; Springer: Berlin, Germany, 1990; pp. 400–417.
42. Langaas, S.; Kane, R. Temporal spectral signatures of fire scars in savanna woodland. In *Remote Sensing: Global Monitoring for Earth Management, Proceedings of the Geoscience and Remote Sensing Symposium, Espoo, Finland, 3–6 June 1991*; IEEE: Piscataway, NJ, USA, 2011; pp. 1157–1160.
43. Fuller, S.P.; Rouse, W.R. Spectral reflectance changes accompanying a post-fire recovery sequence in a subarctic spruce lichen woodland. *Remote Sens. Environ.* **1979**, *8*, 11–23. [[CrossRef](#)]
44. Bowman, D.M.J.S.; Zhang, Y.; Walsh, A.; Williams, R.J. Experimental comparison of four remote sensing techniques to map tropical savanna fire-scars using Landsat-TM imagery. *Int. J. Wildland Fire* **2003**, *12*, 341–348. [[CrossRef](#)]
45. Pereira, J.M. Remote sensing of burned areas in tropical savannas. *Int. J. Wildland Fire* **2003**, *12*, 259–270. [[CrossRef](#)]
46. Chu, T.; Guo, X. Remote sensing techniques in monitoring post-fire effects and patterns of forest recovery in boreal forest regions: A review. *Remote Sens.* **2014**, *6*, 470–520. [[CrossRef](#)]
47. Chen, X.; Vogelmann, J.E.; Rollins, M.; Ohlen, D.; Key, C.H.; Yang, L.; Huang, C.; Shi, H. Detecting post-fire burn severity and vegetation recovery using multitemporal remote sensing spectral indices and field-collected composite burn index data in a ponderosa pine forest. *Int. J. Remote Sens.* **2011**, *32*, 7905–7927. [[CrossRef](#)]
48. Röder, A.; Hill, J.; Duguay, B.; Alloza, J.A.; Vallejo, R. Using long time series of Landsat data to monitor fire events and post-fire dynamics and identify driving factors. A case study in the Ayora region (eastern Spain). *Remote Sens. Environ.* **2008**, *112*, 259–273. [[CrossRef](#)]
49. Roy, D.P.; Boschetti, L.; Justice, C.O.; Ju, J. The collection 5 MODIS burned area product—Global evaluation by comparison with the MODIS active fire product. *Remote Sens. Environ.* **2008**, *112*, 3690–3707. [[CrossRef](#)]
50. Wolfe, R.E.; Roy, D.P.; Vermote, E. Modis land data storage, gridding, and compositing methodology: Level 2 grid. *IEEE Trans. Geosci. Remote Sens.* **1998**, *36*, 1324–1338. [[CrossRef](#)]
51. Schaaf, C.B.; Gao, F.; Strahler, A.H.; Lucht, W.; Li, X.; Tsang, T.; Strugnell, N.C.; Zhang, X.; Jin, Y.; Muller, J.-P. First operational brdf, albedo nadir reflectance products from MODIS. *Remote Sens. Environ.* **2002**, *83*, 135–148. [[CrossRef](#)]

52. Wang, Z.; Schaaf, C.B.; Sun, Q.; Shuai, Y.; Román, M.O. Capturing rapid land surface dynamics with Collection V006 MODIS BRDF/NBAR/Albedo (MCD43) products. *Remote Sens. Environ.* **2018**, *207*, 50–64. [[CrossRef](#)]
53. Friedl, M.A.; Sulla-Menashe, D.; Tan, B.; Schneider, A.; Ramankutty, N.; Sibley, A.; Huang, X. Modis collection 5 global land cover: Algorithm refinements and characterization of new datasets. *Remote Sens. Environ.* **2010**, *114*, 168–182. [[CrossRef](#)]
54. Olson, D.M.; Dinerstein, E.; Wikramanayake, E.D.; Burgess, N.D.; Powell, G.V.; Underwood, E.C.; D’amico, J.A.; Itoua, I.; Strand, H.E.; Morrison, J.C. Terrestrial ecoregions of the world: A new map of life on earth a new global map of terrestrial ecoregions provides an innovative tool for conserving biodiversity. *BioScience* **2001**, *51*, 933–938. [[CrossRef](#)]
55. Pereira, J.C.; Sá, A.L.; Sousa, A.O.; Silva, J.N.; Santos, T.; Carreiras, J.B. Spectral characterisation and discrimination of burnt areas. In *Remote Sensing of Large Wildfires*; Chuvieco, E., Ed.; Springer: Berlin/Heidelberg, Germany, 1999; pp. 123–138.
56. Roy, D.; Lewis, P.; Justice, C. Burned area mapping using multi-temporal moderate spatial resolution data—A bi-directional reflectance model-based expectation approach. *Remote Sens. Environ.* **2002**, *83*, 263–286. [[CrossRef](#)]
57. Stroppiana, D.; Pinnock, S.; Pereira, J.M.C.; Grégoire, J.-M. Radiometric analysis of spot-vegetation images for burnt area detection in northern Australia. *Remote Sens. Environ.* **2002**, *82*, 21–37. [[CrossRef](#)]
58. Key, C.H.; Benson, N.C. Landscape assessment. In *FIREMON: Fire Effects Monitoring and Inventory System*; Department of Agriculture, Forest Service, Rocky Mountain Research Station: Fort Collins, CO, USA, 2006; pp. 1–55.
59. Koutsias, N.; Karteris, M. Logistic regression modelling of multitemporal thematic mapper data for burned area mapping. *Int. J. Remote Sens.* **1998**, *19*, 3499–3514. [[CrossRef](#)]
60. Pereira, M.; Setzer, A. Spectral characteristics of fire scars in Landsat-5 tm images of Amazonia. *Remote Sens.* **1993**, *14*, 2061–2078. [[CrossRef](#)]
61. Huang, H.; Roy, D.; Boschetti, L.; Zhang, H.; Yan, L.; Kumar, S.; Gomez-Dans, J.; Li, J. Separability analysis of sentinel-2a multi-spectral instrument (MSI) data for burned area discrimination. *Remote Sens.* **2016**, *8*, 873. [[CrossRef](#)]
62. Roy, D.P.; Boschetti, L.; Giglio, L. Remote sensing of global savanna fire occurrence, extent, and properties. In *Ecosystem Function in Savannas: Measurement and Modeling at Landscape to Global Scales*; Taylor & Francis Group: Abingdon, UK, 2010; p. 239.
63. Wang, Z.; Schaaf, C.B.; Chopping, M.J.; Strahler, A.H.; Wang, J.; Román, M.O.; Rocha, A.V.; Woodcock, C.E.; Shuai, Y. Evaluation of moderate-resolution imaging spectroradiometer (MODIS) snow albedo product (mcd43a) over tundra. *Remote Sens. Environ.* **2012**, *117*, 264–280. [[CrossRef](#)]
64. Goodwin, N.R.; Coops, N.C.; Wulder, M.A.; Gillanders, S.; Schroeder, T.A.; Nelson, T. Estimation of insect infestation dynamics using a temporal sequence of Landsat data. *Remote Sens. Environ.* **2008**, *112*, 3680–3689. [[CrossRef](#)]
65. Loboda, T.V.; French, N.H.F.; Hight-Harf, C.; Jenkins, L.; Miller, M.E. Mapping fire extent and burn severity in alaskan tussock tundra: An analysis of the spectral response of tundra vegetation to wildland fire. *Remote Sens. Environ.* **2013**, *134*, 194–209. [[CrossRef](#)]
66. Chuvieco, E.; Martin, M.P.; Palacios, A. Assessment of different spectral indices in the red-near-infrared spectral domain for burned land discrimination. *Int. J. Remote Sens.* **2002**, *23*, 5103–5110. [[CrossRef](#)]
67. Koutsias, N.; Karteris, M. Burned area mapping using logistic regression modeling of a single post-fire Landsat-5 thematic mapper image. *Int. J. Remote Sens.* **2000**, *21*, 673–687. [[CrossRef](#)]
68. Chuvieco, E.; Congalton, R.G. Mapping and inventory of forest fires from digital processing of TM data. *Geocarto Int.* **1988**, *3*, 41–53. [[CrossRef](#)]
69. Bastarrika, A.; Chuvieco, E.; Martín, M.P. Mapping burned areas from Landsat TM/ETM+ data with a two-phase algorithm: Balancing omission and commission errors. *Remote Sens. Environ.* **2011**, *115*, 1003–1012. [[CrossRef](#)]
70. Mitri, G.; Gitas, I. A semi-automated object-oriented model for burned area mapping in the Mediterranean region using Landsat-TM imagery. *Int. J. Wildland Fire* **2004**, *13*, 367–376. [[CrossRef](#)]
71. Miller, J.D.; Yool, S.R. Mapping forest post-fire canopy consumption in several overstorey types using multi-temporal Landsat TM and ETM data. *Remote Sens. Environ.* **2002**, *82*, 481–496. [[CrossRef](#)]

72. Hudak, A.; Brockett, B. Mapping fire scars in a southern African savannah using Landsat imagery. *Int. J. Remote Sens.* **2004**, *25*, 3231–3243. [[CrossRef](#)]
73. Silva, J.M.; Sá, A.C.; Pereira, J.M. Comparison of burned area estimates derived from spot-vegetation and Landsat ETM+ data in Africa: Influence of spatial pattern and vegetation type. *Remote Sens. Environ.* **2005**, *96*, 188–201. [[CrossRef](#)]
74. Smith, A.M.S.; Drake, N.A.; Wooster, M.J.; Hudak, A.T.; Holden, Z.A.; Gibbons, C.J. Production of Landsat ETM+ reference imagery of burned areas within southern African savannahs: Comparison of methods and application to MODIS. *Int. J. Remote Sens.* **2007**, *28*, 2753–2775. [[CrossRef](#)]
75. Stroppiana, D.; Boschetti, M.; Zaffaroni, P.; Brivio, P.A. Analysis and interpretation of spectral indices for soft multicriteria burned-area mapping in Mediterranean regions. *IEEE Geosci. Remote Sens. Lett.* **2009**, *6*, 499–503. [[CrossRef](#)]
76. Key, C.; Benson, N. Measuring and remote sensing of burn severity. In *Proceedings of the US Geological Survey Wildland Fire Workshop, Los Alamos, NM, USA, 31 October–3 November 2000*; Open-File Report 2002-11; US Geological Survey: Washington, DC, USA, 2000.
77. Fraser, R.; Fernandes, R.; Latifovic, R. Multi-temporal mapping of burned forest over Canada using satellite-based change metrics. *Geocarto Int.* **2003**, *18*, 37–47. [[CrossRef](#)]
78. Henry, M.C. Comparison of single-and multi-date Landsat data for mapping wildfire scars in Ocala national forest, Florida. *Photogramm. Eng. Remote Sens.* **2008**, *74*, 881–891. [[CrossRef](#)]
79. Escuin, S.; Navarro, R.; Fernández, P. Fire severity assessment by using NBR (normalized burn ratio) and NDVI (normalized difference vegetation index) derived from Landsat TM/ETM images. *Int. J. Remote Sens.* **2008**, *29*, 1053–1073. [[CrossRef](#)]
80. Krawchuk, M.A.; Moritz, M.A. Constraints on global fire activity vary across a resource gradient. *Ecology* **2011**, *92*, 121–132. [[CrossRef](#)] [[PubMed](#)]
81. Moritz, M.A.; Parisien, M.-A.; Batllori, E.; Krawchuk, M.A.; Van Dorn, J.; Ganz, D.J.; Hayhoe, K. Climate change and disruptions to global fire activity. *Ecosphere* **2012**, *3*, 1–22. [[CrossRef](#)]
82. Boschetti, L.; Roy, D.P. Defining a fire year for reporting and analysis of global interannual fire variability. *J. Geophys. Res. Biogeosci.* **2008**, *113*. [[CrossRef](#)]
83. Giglio, L.; Csiszar, I.; Justice, C.O. Global distribution and seasonality of active fires as observed with the terra and aqua moderate resolution imaging spectroradiometer (MODIS) sensors. *J. Geophys. Res. Biogeosci.* **2006**, *111*. [[CrossRef](#)]
84. Archibald, S.; Lehmann, C.E.R.; Gómez-Dans, J.L.; Bradstock, R.A. Defining pyromes and global syndromes of fire regimes. *Proc. Natl. Acad. Sci. USA* **2013**, *110*, 6442–6447. [[CrossRef](#)] [[PubMed](#)]
85. Lambin, E.F.; Goyvaerts, K.; Petit, C. Remotely-sensed indicators of burning efficiency of savannah and forest fires. *Int. J. Remote Sens.* **2003**, *24*, 3105–3118. [[CrossRef](#)]
86. Schwartz, M.D.; Reed, B.C. Surface phenology and satellite sensor-derived onset of greenness: An initial comparison. *Int. J. Remote Sens.* **1999**, *20*, 3451–3457. [[CrossRef](#)]
87. White, M.A.; Thornton, P.E.; Running, S.W. A continental phenology model for monitoring vegetation responses to interannual climatic variability. *Glob. Biogeochem. Cycles* **1997**, *11*, 217–234. [[CrossRef](#)]
88. Dwyer, E.; Pereira, J.; Grégoire, J.M.; DaCamara, C.C. Characterization of the spatio-temporal patterns of global fire activity using satellite imagery for the period April 1992 to March 1993. *J. Biogeogr.* **2000**, *27*, 57–69. [[CrossRef](#)]
89. Bucini, G.; Lambin, E.F. Fire impacts on vegetation in central Africa: A remote-sensing-based statistical analysis. *Appl. Geogr.* **2002**, *22*, 27–48. [[CrossRef](#)]
90. Lefsky, M.A. A global forest canopy height map from the moderate resolution imaging spectroradiometer and the geoscience laser altimeter system. *Geophys. Res. Lett.* **2010**, *37*. [[CrossRef](#)]
91. Schipper, J.; Chanson, J.S.; Chiozza, F.; Cox, N.A.; Hoffmann, M.; Katariya, V.; Lamoreux, J.; Rodrigues, A.S.L.; Stuart, S.N.; Temple, H.J.; et al. The status of the world's land and marine mammals: Diversity, threat, and knowledge. *Science* **2008**, *322*, 225–230. [[CrossRef](#)] [[PubMed](#)]
92. Guenther, C.C. Estimates of global terrestrial isoprene emissions using MEGAN (model of emissions of gases and aerosols from nature). *Atmos. Chem. Phys.* **2006**, *6*, 3181–3210. [[CrossRef](#)]
93. Loarie, S.R.; Duffy, P.B.; Hamilton, H.; Asner, G.P.; Field, C.B.; Ackerly, D.D. The velocity of climate change. *Nature* **2009**, *462*, 1052–1055. [[CrossRef](#)] [[PubMed](#)]

94. Schneider, A.; Friedl, M.A.; Potere, D. A new map of global urban extent from MODIS satellite data. *Environ. Res. Lett.* **2009**, *4*, 044003. [[CrossRef](#)]
95. DeFries, R.S.; Rudel, T.; Uriarte, M.; Hansen, M. Deforestation driven by urban population growth and agricultural trade in the twenty-first century. *Nat. Geosci.* **2010**, *3*, 178–181. [[CrossRef](#)]
96. Boschetti, L.; Stehman, S.V.; Roy, D.P. A stratified random sampling design in space and time for regional to global scale burned area product validation. *Remote Sens. Environ.* **2016**, *186*, 465–478. [[CrossRef](#)]
97. Padilla, M.; Stehman, S.V.; Chuvieco, E. Validation of the 2008 MODIS-MCD45 global burned area product using stratified random sampling. *Remote Sens. Environ.* **2014**, *144*, 187–196. [[CrossRef](#)]
98. Dixon, R.K.; Solomon, A.M.; Brown, S.; Houghton, R.A.; Trexler, M.C.; Wisniewski, J. Carbon pools and flux of global forest ecosystems. *Science* **1994**, *263*, 185–190. [[CrossRef](#)] [[PubMed](#)]
99. Lasko, K.; Vadrevu, K.P.; Tran, V.T.; Ellicott, E.; Nguyen, T.T.; Bui, H.Q.; Justice, C. Satellites may underestimate rice residue and associated burning emissions in Vietnam. *Environ. Res. Lett.* **2017**, *12*, 085006. [[CrossRef](#)]
100. Hall, J.V.; Loboda, T.V.; Giglio, L.; McCarty, G.W. A MODIS-based burned area assessment for Russian croplands: Mapping requirements and challenges. *Remote Sens. Environ.* **2016**, *184*, 506–521. [[CrossRef](#)]
101. Vanderhoof, M.; Brunner, N.; Beal, Y.-J.; Hawbaker, T. Evaluation of the U.S. Geological survey Landsat burned area essential climate variable across the conterminous U.S. Using commercial high-resolution imagery. *Remote Sens.* **2017**, *9*, 743. [[CrossRef](#)]
102. Engel, E.C.; Abella, S.R. Vegetation recovery in a desert landscape after wildfires: Influences of community type, time since fire and contingency effects. *J. Appl. Ecol.* **2011**, *48*, 1401–1410. [[CrossRef](#)]
103. West, N.E.; Hassan, M.A. Recovery of sagebrush-grass vegetation following wildfire. *J. Range Manag.* **1985**, *38*, 131–134. [[CrossRef](#)]
104. Meney, K.A.; Nielssen, G.M.; Dixon, K.W. Seed bank patterns in Restionaceae and Epacridaceae after wildfire in kwongan in southwestern Australia. *J. Veg. Sci.* **1994**, *5*, 5–12. [[CrossRef](#)]
105. Cochrane, M.A. Fire science for rainforests. *Nature* **2003**, *421*, 913–919. [[CrossRef](#)] [[PubMed](#)]
106. Verhegghen, A.; Eva, H.; Ceccherini, G.; Achard, F.; Gond, V.; Gourlet-Fleury, S.; Cerutti, P. The potential of sentinel satellites for burnt area mapping and monitoring in the Congo basin forests. *Remote Sens.* **2016**, *8*, 986. [[CrossRef](#)]
107. Cochrane, M.A.; Alencar, A.; Schulze, M.D.; Souza, C.M.; Nepstad, D.C.; Lefebvre, P.; Davidson, E.A. Positive feedbacks in the fire dynamic of closed canopy tropical forests. *Science* **1999**, *284*, 1832–1835. [[CrossRef](#)] [[PubMed](#)]
108. Kumar, S.S.; Roy, D.P.; Cochrane, M.A.; Souza, C.M.; Barber, C.P.; Boschetti, L. A quantitative study of the proximity of satellite detected active fires to roads and rivers in the Brazilian tropical moist forest biome. *Int. J. Wildland Fire* **2014**, *23*, 532–543. [[CrossRef](#)]
109. Eva, H.; Lambin, E.F. Fires and land-cover change in the tropics: A remote sensing analysis at the landscape scale. *J. Biogeogr.* **2000**, *27*, 765–776. [[CrossRef](#)]
110. Tovar, C.; Breman, E.; Brncic, T.; Harris, D.J.; Bailey, R.; Willis, K.J. Influence of 1100 years of burning on the central African rainforest. *Ecography* **2014**, *37*, 1139–1148. [[CrossRef](#)]
111. Hope, G.; Kershaw, A.P.; Kaars, S.V.D.; Xiangjun, S.; Liew, P.-M.; Heusser, L.E.; Takahara, H.; McGlone, M.; Miyoshi, N.; Moss, P.T. History of vegetation and habitat change in the Austral-Asian region. *Quat. Int.* **2004**, *118–119*, 103–126. [[CrossRef](#)]
112. Morton, D.C.; DeFries, R.S.; Nagol, J.; Souza, C.M., Jr.; Kasischke, E.S.; Hurtt, G.C.; Dubayah, R. Mapping canopy damage from understory fires in amazon forests using annual time series of Landsat and MODIS data. *Remote Sens. Environ.* **2011**, *115*, 1706–1720. [[CrossRef](#)]
113. Chen, D.; Pereira, J.M.C.; Masiero, A.; Pirotti, F. Mapping fire regimes in china using MODIS active fire and burned area data. *Appl. Geogr.* **2017**, *85*, 14–26. [[CrossRef](#)]
114. Close, D.C.; Davidson, N.J.; Johnson, D.W.; Abrams, M.D.; Hart, S.C.; Lunt, I.D.; Archibald, R.D.; Horton, B.; Adams, M.A. Premature decline of eucalyptus and altered ecosystem processes in the absence of fire in some Australian forests. *Bot. Rev.* **2009**, *75*, 191–202. [[CrossRef](#)]
115. Westerling, A.L.; Hidalgo, H.G.; Cayan, D.R.; Swetnam, T.W. Warming and earlier spring increase western US forest wildfire activity. *Science* **2006**, *313*, 940–943. [[CrossRef](#)] [[PubMed](#)]

116. Clark, J.S.; Iverson, L.; Woodall, C.W.; Allen, C.D.; Bell, D.M.; Bragg, D.C.; D'Amato, A.W.; Davis, F.W.; Hersh, M.H.; Ibanez, I.; et al. The impacts of increasing drought on forest dynamics, structure, and biodiversity in the United States. *Glob. Chang. Biol.* **2016**, *22*, 2329–2352. [[CrossRef](#)] [[PubMed](#)]
117. Slocum, M.G.; Platt, W.J.; Cooley, H.C. Effects of differences in prescribed fire regimes on patchiness and intensity of fires in subtropical savannas of Everglades National Park, Florida. *Restor. Ecol.* **2003**, *11*, 91–102. [[CrossRef](#)]
118. Glitzenstein, J.S.; Platt, W.J.; Streng, D.R. Effects of fire regime and habitat on tree dynamics in north Florida longleaf pine savannas. *Ecol. Monogr.* **1995**, *65*, 441–476. [[CrossRef](#)]
119. Li, M.S.; Mao, L.J.; Lu, C.; Wang, Y. Temporal change in fragmentation in China's primary forest ecoregions. In *Advanced Materials Research*; Trans Tech Publ.: Zurich, Switzerland, 2012; pp. 1286–1296.
120. Wierzchowski, J.; Heathcott, M.; Flannigan, M.D. Lightning and lightning fire, central cordillera, Canada. *Int. J. Wildland Fire* **2002**, *11*, 41–51. [[CrossRef](#)]
121. De Groot, W.J.; Cantin, A.S.; Flannigan, M.D.; Soja, A.J.; Gowman, L.M.; Newbery, A. A comparison of Canadian and Russian boreal forest fire regimes. *For. Ecol. Manag.* **2013**, *294*, 23–34. [[CrossRef](#)]
122. Burrows, N.D.; Burbidge, A.A.; Fuller, P.J.; Behn, G. Evidence of altered fire regimes in the western desert region of Australia. *Conserv. Sci. West. Aust.* **2006**, *5*, 14.
123. Houghton, R.A.; Hackler, J.L. Emissions of carbon from land use change in sub-Saharan Africa. *J. Geophys. Res. Biogeosci.* **2006**, *111*. [[CrossRef](#)]
124. Mishra, N.B.; Mainali, K.P.; Crews, K.A. Modelling spatiotemporal variability in fires in semiarid savannas: A satellite-based assessment around Africa's largest protected area. *Int. J. Wildland Fire* **2016**, *25*, 730–741. [[CrossRef](#)]
125. Grégoire, J.-M.; Simonetti, D. Interannual changes of fire activity in the protected areas of the sun network and other parks and reserves of the west and central Africa region derived from MODIS observations. *Remote Sens.* **2010**, *2*, 446–463. [[CrossRef](#)]
126. Staver, A.C.; Archibald, S.; Levin, S.A. The global extent and determinants of savanna and forest as alternative biome states. *Science* **2011**, *334*, 230–232. [[CrossRef](#)] [[PubMed](#)]
127. Bond, W.J.; Keeley, J.E. Fire as a global 'herbivore': The ecology and evolution of flammable ecosystems. *Trends Ecol. Evol.* **2005**, *20*, 387–394. [[CrossRef](#)] [[PubMed](#)]
128. Van der Werf, G.R.; Randerson, J.T.; Giglio, L.; Gobron, N.; Dolman, A.J. Climate controls on the variability of fires in the tropics and subtropics. *Glob. Biogeochem. Cycles* **2008**, *22*. [[CrossRef](#)]
129. Roy, D.; Landmann, T. Characterizing the surface heterogeneity of fire effects using multi-temporal reflective wavelength data. *Int. J. Remote Sens.* **2005**, *26*, 4197–4218. [[CrossRef](#)]
130. Scholes, R.J.; Walker, B.H. *An African Savanna: Synthesis of the Nylsvey Study*; Cambridge University Press: Cambridge, UK, 2004.
131. Eva, H.; Lambin, E. Burnt area mapping in central Africa using ATSR data. *Int. J. Remote Sens.* **1998**, *19*, 3473–3497. [[CrossRef](#)]
132. Cheney, N.; Gould, J.; Catchpole, W. The influence of fuel, weather and fire shape variables on fire-spread in grasslands. *Int. J. Wildland Fire* **1993**, *3*, 31–44. [[CrossRef](#)]
133. Gill, A.M.; Moore, P.H.R.; Williams, R.J. Fire weather in the wet-dry tropics of the World Heritage Kakadu National Park, Australia. *Aust. J. Ecol.* **1996**, *21*, 302–308. [[CrossRef](#)]
134. Williams, R.J.; Cook, G.D.; Gill, A.M.; Moore, P.H.R. Fire regime, fire intensity and tree survival in a tropical savanna in northern Australia. *Aust. J. Ecol.* **1999**, *24*, 50–59. [[CrossRef](#)]
135. Littell, J.S.; McKenzie, D.; Peterson, D.L.; Westerling, A.L. Climate and wildfire area burned in western U.S. Ecoregions, 1916–2003. *Ecol. Appl.* **2009**, *19*, 1003–1021. [[CrossRef](#)] [[PubMed](#)]
136. McCarty, J.L.; Ellicott, E.A.; Romanenkov, V.; Rukhovitch, D.; Koroleva, P. Multi-year black carbon emissions from cropland burning in the Russian federation. *Atmos. Environ.* **2012**, *63*, 223–238. [[CrossRef](#)]
137. Wessman, C.A.; Bateson, C.A.; Benning, T.L. Detecting fire and grazing patterns in tallgrass prairie using spectral mixture analysis. *Ecol. Appl.* **1997**, *7*, 493–511. [[CrossRef](#)]
138. Lu, B.; He, Y. Analyzing a north American prairie wildfire using remote sensing imagery. In Proceedings of the 2014 IEEE Geoscience and Remote Sensing Symposium, Quebec City, QC, Canada, 13–18 July 2014; pp. 832–835.

139. Mohler, R.L.; Goodin, D.G. Identifying a suitable combination of classification technique and bandwidth(s) for burned area mapping in tallgrass prairie with MODIS imagery. *Int. J. Appl. Earth Obs. Geoinf.* **2012**, *14*, 103–111. [[CrossRef](#)]



© 2018 by the authors. Licensee MDPI, Basel, Switzerland. This article is an open access article distributed under the terms and conditions of the Creative Commons Attribution (CC BY) license (<http://creativecommons.org/licenses/by/4.0/>).